Geochemistry Geophysics Geosystems G3
AN ELECTRONIC JOURNAL OF THE EARTH SCIENCES
Published by AGU and the Geochemical Society

Article
Volume 10, Number 5
27 May 2009
Q05S15, doi:10.1029/2009GC002375
ISSN: 1525-2027

Shear wave anisotropy beneath Nicaragua and Costa Rica: Implications for flow in the mantle wedge

David L. Abt and Karen M. Fischer
Department of Geological Sciences, Brown University, Providence, Rhode Island 02912, USA (david_abt@brown.edu)

Geoffrey A. Abers
Department of Earth Sciences, Boston University, Boston, Massachusetts 02215 USA

Now at Lamont-Doherty Earth Observatory, Earth Institute at Columbia University, Palisades, New York 10964, USA

Wilfried Strauch
Dirección General de Geofísica, Instituto Nicaragüense de Estudios Territoriales, Managua, Nicaragua

J. Marino Protti and Victor González
Observatorio Vulcanológico y Sismológico de Costa Rica, Universidad Nacional, Apartado 2346-3000, Heredia 40101, Costa Rica

[1] We present new shear wave splitting data from local events in Costa Rica and Nicaragua recorded by the temporary (July 2004 to March 2006) 48-station TUCAN broadband seismic array. Observed fast polarization directions in the fore arc, arc, and back arc range from arc-parallel to arc-normal over very short distances (<5 km when plotted at raypath midpoints) making the direct interpretation of individual splitting measurements in terms of flow tenuous, even when considering variations in the relationship between lattice-preferred orientation and deformation (e.g., B-type dislocation creep in olivine). Therefore, we tomographically invert the splitting measurements to find a three-dimensional model of crystallographic orientation in the wedge. We assume the elastic constants of olivine and orthopyroxene with hexagonal symmetry and use a damped, iterative least squares approach to account for the nonlinear behavior of splitting when considering three-dimensional ray propagation and distributions of anisotropy. The best fitting model contains roughly horizontal, arc-parallel olivine [100] axes in the mantle wedge down to at least 125 km beneath the back arc and arc, which we interpret to indicate along-arc flow in the mantle wedge. Pb and Nd isotopic ratios in arc lavas provide additional evidence for arc-parallel flow and also constrain the direction (northwest, from Costa Rica to Nicaragua) and minimum flow rate (63–190 mm/a). With only slightly oblique subduction at 85 mm/a of the relatively planar Cocos Plate, the most likely mechanism for driving along-arc transport is toroidal flow around the edge of the slab in southern Costa Rica, generated by greater slab rollback in Nicaragua. Two important implications of this arc-parallel flow are the progressive depletion of the mantle source for arc lavas from Costa Rica to Nicaragua and the possible need for significant decoupling between the wedge and downgoing plate.

Components: 15,269 words, 15 figures.

Keywords: shear wave splitting; tomography; anisotropy; Central America; subduction.

Index Terms: 7240 Seismology: Subduction zones (1207, 1219, 1240); 7270 Seismology: Tomography (6982, 8180); 8104 Tectonophysics: Continental margins: convergent.

Received 5 January 2009; **Revised** 25 March 2009; **Accepted** 9 April 2009; **Published** 27 May 2009.

Abt, D. L., K. M. Fischer, G. A. Abers, W. Strauch, J. M. Protti, and V. González (2009), Shear wave anisotropy beneath Nicaragua and Costa Rica: Implications for flow in the mantle wedge, *Geochem. Geophys. Geosyst.*, *10*, Q05S15, doi:10.1029/2009GC002375.

Theme: Central American Subduction System
Guest Editors: G. Alvarado, K. Hoernle, and E. Silver

1. Introduction

[2] The pattern of solid mantle flow in subduction zones fundamentally influences wedge thermal structure, melt generation and transport, and slab dynamics. Seismic anisotropy offers a means of imaging mantle wedge flow, and a growing database of shear wave splitting measurements from subduction zones [e.g., *Wiens and Smith*, 2003; *Pozgay et al.*, 2007; *Long and Silver*, 2008] has revealed flow patterns that are considerably more complex than those predicted by 2-D entrainment of the wedge with the downgoing plate (2-D corner flow) [e.g., *McKenzie*, 1979; *Ribe*, 1989; *Fischer et al.*, 2000; *Blackman and Kendall*, 2002; *Lassak et al.*, 2006]. This conclusion holds true when the [100] axis of olivine is assumed to align parallel to flow, as suggested by experimentally and naturally deformed dunites and harzburgites at relatively dry conditions [e.g., *Zhang and Karato*, 1995; *Ismaïl and Mainprice*, 1998], or when taking into account recent deformation experiments [*Bystricky et al.*, 2000; *Jung and Karato*, 2001; *Holtzman et al.*, 2003; *Mainprice et al.*, 2005; *Jung et al.*, 2006; *Katayama and Karato*, 2006] and field observations [*Mehl et al.*, 2003; *Mizukami et al.*, 2004] that have shown olivine fabrics depend on pressure, temperature, melt and water content, and stress.

[3] For example, in the Japan and Ryukyu subduction zones, a shift from arc-parallel (perpendicular to plate motion) fast directions in the fore arc to arc-normal (plate motion parallel) fast directions in the back arc is observed in both local S [*Long and van der Hilst*, 2006; *Nakajima et al.*, 2006] and teleseismic SKS [*Long and van der Hilst*, 2005] splitting measurements. This pattern is consistent with 2-D corner flow, if a B-type fabric [*Jung and Karato*, 2001; *Jung et al.*, 2006] exists in the cold wedge corner [*Kneller et al.*, 2005]. However, in other subduction zones, fast directions are arc-parallel or vary from arc-parallel to arc-normal for paths that sample the wedge well outside its cold corner, indicating significantly 3-D flow [*Wiens and Smith*, 2003; *Long and Silver*, 2008]. Examples include South America [*Russo and Silver*, 1994; *Polet et al.*, 2000; *Anderson et al.*, 2004; M. L. Anderson et al., Along-strike mantle flow variations in a segment of the South American subduction zone, Chile and Argentina, submitted to *Earth and Planetary Science Letters*, 2009], New Zealand [*Matcham et al.*, 2000; *Audoine et al.*, 2004; *Morley et al.*, 2006], Tonga-Fiji [*Smith et al.*, 2001], Taiwan [*Huang et al.*, 2006], the Marianas [*Pozgay et al.*, 2007], Izu-Bonin [*Anglin and Fouch*, 2005], Kamchatka [*Peyton et al.*, 2001; *Levin et al.*, 2004], the Aleutians [*Yang et al.*, 1995], Alaska [*Christensen et al.*, 2003], and Central America [*Hoernle et al.*, 2008; this paper].

[4] Physical factors that could contribute to 3-D flow include oblique convergence [*Hall et al.*, 2000], trench retreat [*Buttles and Olsen*, 1998; *Kincaid and Griffiths*, 2004; *Funiciello et al.*, 2006], slab edges [*Kincaid and Griffiths*, 2003; *Funiciello et al.*, 2006] or tears, upper plate deformation or delamination [*Hall et al.*, 2000; *Blackman and Kendall*, 2002; *Kincaid and Hall*, 2003, *Lowman et al.*, 2007; *Behn et al.*, 2007], nonplanar slab geometry [*Kneller and van Keken*, 2007], and a low-viscosity wedge channel [*Conder and Wiens*, 2007]. In addition, shape-preferred orientation (SPO), the alignment of heterogeneous features such as melt or fluid-filled cracks within the mantle and lithosphere/crust, should be accounted for when interpreting measurements of anisotropy in complex regions such as subduction zones.

[5] In this study we present shear wave splitting measurements from waveforms collected by the Tomography Under Costa Rica and Nicaragua (TUCAN) Broadband Seismic Experiment (Figure 1) and a 3-D model for anisotropy in the Nicaragua–Costa Rica subduction zone obtained by inverting the splitting measurements using a new tomograph-

ic approach [*Abt and Fischer*, 2008]. Our objective was to place constraints on the pattern of wedge flow, and we find evidence for significant anisotropy with a fast symmetry axis parallel to the arc in the mantle beneath the arc and back arc. These results, when combined with Pb and Nd isotope data (discussed in Section 2), strongly suggest along-arc flow to the northwest in the mantle wedge beneath Nicaragua and Costa Rica [*Hoernle et al.*, 2008]. Although the 3-D anisotropic model has been previously published [*Hoernle et al.*, 2008], in this study we explore its uniqueness and implications in greater depth.

2. Tectonic and Geochemical Variations Across Nicaragua and Costa Rica

[6] The Nicaragua–Costa Rica subduction zone offers a unique environment to investigate geodynamic, seismogenic, and petrophysical processes in the mantle wedge because distinct changes in arc lava geochemistry, seismic activity, and geomorphology are observed over a relatively short distance (~500 km). Here we review features of the tectonic setting that are particularly relevant to understanding regional mantle flow.

[7] The Cocos Plate, which is subducting beneath the southwestern edge of the Caribbean and North American plates (Figure 1), formed at both the East Pacific Rise (EPR) and the Galapagos Spreading Center (GSC). Seafloor magnetic anomalies place the junction between these two components of the Cocos plate at the southern end of the Nicoya Peninsula. Convergence occurs at a rate of ~85 mm/a, with obliquity varying from ~7° in central Costa Rica to ~17° in Nicaragua [*Barckhausen et al.*, 2001; *DeMets*, 2001].

[8] The shape of the subducting slab may be an important driver for subduction zone flow, and along-strike changes in Cocos slab shape have been suggested [*Protti et al.*, 1994; *Husen et al.*, 2003; *Syracuse and Abers*, 2006]. However, velocity tomography and hypocentral relocation using data from the TUCAN array [*Syracuse et al.*, 2008] indicates that the slab below 50 km depth dips at 50–60° beneath most of Nicaragua and Costa Rica, with a moderate shallowing of slab dip to roughly 45° beneath the southeastern end of the array in central Costa Rica. No resolvable change in slab geometry occurs where the arc shifts 40 km further from the trench at the Nicaragua–Costa Rica border. In southeastern Costa Rica, significant thrust faulting occurs in the absence of large-volume arc volcanism [*Carr et al.*, 2003] and deep Cocos Plate–related seismicity [*Protti et al.*, 1994]. *Abratis and Wörner* [2001] contend that the lack of deep seismicity, a unique progression of arc geochemistry, and shallow subduction represent the opening of a slab window caused by the subduction of the Cocos Ridge, allowing Galapagos hot spot-enriched mantle to pass into the Caribbean side of the subduction zone. Another reasonable explanation for the termination of volcanism and deep seismicity would be that this is the location of the slab edge, with the absence of a lithospheric barrier between Cocos-Nazca (i.e., Pacific) upper mantle and Caribbean (i.e., Atlantic) upper mantle [e.g., *Russo and Silver*, 1994]. In addition, trench motion (e.g., slab rollback during trench retreat) near the slab edge could produce a prominent deviation from a simple 2-D corner flow pattern [*Kincaid and Griffiths*, 2003, 2004]. Estimates of trench motion in Central America vary depending on the plate motion model used from roughly 2 cm/a of trench retreat to 2.5 cm/a of trench advance [*Lallemand et al.*, 2008; *Schellart et al.*, 2008]. However, for plate motion models where along-arc variations in trench motion exist, the trench in northern Nicaragua tends to be moving seaward relative to the trench in southern Costa Rica [*Schellart et al.*, 2008].

[9] A variety of upper plate features have been proposed as evidence for the evolution of slab shape and subduction zone flow. Overall, the position of the arc has migrated trenchward (roughly southwest) since the early Miocene, with the largest offsets near the northern border of Nicaragua with Honduras [*Weinberg*, 1992; *Plank et al.*, 2002; *Alvarado et al.*, 2007]. Since the middle Miocene, the arc has been relatively stationary in Costa Rica, but continued trenchward offsets occurred in Nicaragua [*Weinberg*, 1992; *Plank et al.*, 2002], and have been attributed to slab rollback or an increase in subduction angle [*Weinberg*, 1992]. These changes in arc position are consistent with the trench migration pattern in the work by *Schellart et al.* [2008]. The recent and present-day arc in Nicaragua is located in the Nicaragua Depression, a large lowland area containing Lake Managua and Lake Nicaragua. Sediment thicknesses have been estimated at 2 to 2.5 km from potential field data [*Elming and Rasmussen*, 1997] and at roughly 3 km from receiver function modeling of TUCAN Ps waveforms [*MacKenzie et al.*, 2008]. *Weinberg* [1992] proposed that the 50-km-wide depression

formed in the Pliocene to Middle Pleistocene, possibly as a dynamic response of the upper plate to slab steepening.

[10] However, despite this history, recent extension and subsidence appear to be small. GPS data indicate that present-day upper plate deformation is dominated by the northwestward translation of a fore-arc sliver that includes the Nicoya Peninsula and the Pacific coast of Nicaragua [*Lundgren et al.*, 1999; *Iinuma et al.*, 2004; *Norabuena et al.*, 2004; *Turner et al.*, 2007] at rates of 7–8 mm/a in Costa Rica [*Norabuena et al.*, 2004] and an average of 15 mm/a in Nicaragua [*Turner et al.*, 2007]. Arc-normal extension occurs only northwest of Lake Managua (5 mm/a on average) with a small component of arc-normal compression in southeastern Nicaragua [*Turner et al.*, 2007]; again, such a pattern is consistent with the signs of the differential trench motion rates estimated by *Schellart et al.* [2008]. In regard to recent subsidence, data from a borehole on Momotombo volcano in the middle of the Nicaragua Depression indicated only 150 m of Quaternary volcaniclastic sediments on top of Tertiary volcanics [*van Wyk de Vries*, 1993].

[11] Geochemical and isotopic variations also exist along strike in this subduction zone. The presence of Ocean Island Basalt (OIB) signatures related to the Galapagos plume in Costa Rican and Nicaraguan arc magmas is particularly relevant to anisotropy, as it has been used to argue for flow in the mantle wedge parallel to the slab. Proposed scenarios include flow of Pacific mantle from beneath the Nazca slab in South America that enters the wedge beneath Panama [*Russo and Silver*, 1994; *Herrstrom et al.*, 1995] or flow into the wedge from a slab window beneath central Costa Rica [*Abratis and Wörner*, 2001]. Alternative models invoke melting of mantle that was influenced by the Galapagos plume during the Cretaceous formation of the Caribbean Large Igneous Province [*Feigenson et al.*, 2004], or melting of eroded fore-arc complexes that had been accreted from the Cocos Ridge [*Goss and Kay*, 2006]. Recently, mixing trends defined by $^{208}Pb/^{204}Pb$ and $^{143}Nd/^{144}Nd$ ratios have pointed to the Galapagos seamounts, which are subducting beneath central Costa Rica (Figure 1), as the source of the OIB signature in volcanic front magmas from central Costa Rica and Nicaragua [*Hoernle et al.*, 2008]. This model indicates northwest flow in the mantle wedge at a minimum velocity of 63–190 mm/a [*Hoernle et al.*, 2008], whereas the *Abratis and Wörner* [2001] model implies flow at roughly 40 mm/a. Regardless, both rates are significant relative to the rate of subducting plate motion (~85 mm/a [*DeMets*, 2001]).

3. Shear Wave Splitting Observations

[12] We analyze shear wave splitting from local events, and this approach has both advantages and disadvantages for studying anisotropy in the mantle wedge. Unlike SKS waves, which are sensitive to anisotropy from the core-mantle boundary to the station, local S waves, generated by earthquakes in the subducting slab, sample anisotropy only in the slab itself, the mantle wedge, and the overriding lithosphere and crust. Incidence angles for SKS waves are typically close to vertical, but for local phases they can range from vertical to nearly horizontal. However, in order to avoid waveform complications from the free surface and shallow interface phase shifts and converted phases, we restrict our analysis to events within the "shear wave window" (<35° from vertical for straight-line raypaths). Because shear wave splitting is dependent on propagation (and polarization) direction, this broader range of incidence angles (even when limited to the shear wave window) allows local S

Figure 1. The TUCAN study region is located at the southeast end of the Central American subduction zone. (top) The Cocos Plate forms at both the East Pacific Rise (EPR) and the Cocos-Nazca Spreading Center (CNSC) and then subducts beneath the North American and Caribbean plates at the Middle America Trench. (bottom) The enlarged area shows the seismic stations used in the splitting analysis, as well as some of the important tectonic features of the region. These include the difference in Cocos Plate age and source ridge across the trace of the triple junction (thick dashed black line) [*Barckhausen et al.*, 2001]; the termination of deep, subduction related seismicity in southern Costa Rica [*Protti et al.*, 1994]; an apparent bend in the slab beneath northern Costa Rica [*Protti et al.*, 1994; *Syracuse et al.*, 2008]; and the change in obliquity of subduction along strike of the trench [*DeMets*, 2001]. Each of these features may kinematically influence the pattern of flow in the mantle wedge and, therefore, must be considered when interpreting flow from anisotropy. The subducting seamount province and Cocos Ridge, discussed in section 2 and by *Hoernle et al.* [2008], are highlighted in red and blue, respectively. To maintain legibility, we label only station N8 in the Nicaraguan cross-arc line for reference to the splitting example in Figure 2 (green circle is event location, and gray line is raypath for the example). LM, Lake Managua; LN, Lake Nicaragua; MV, Momotombo Volcano; NP, Nicoya Peninsula.

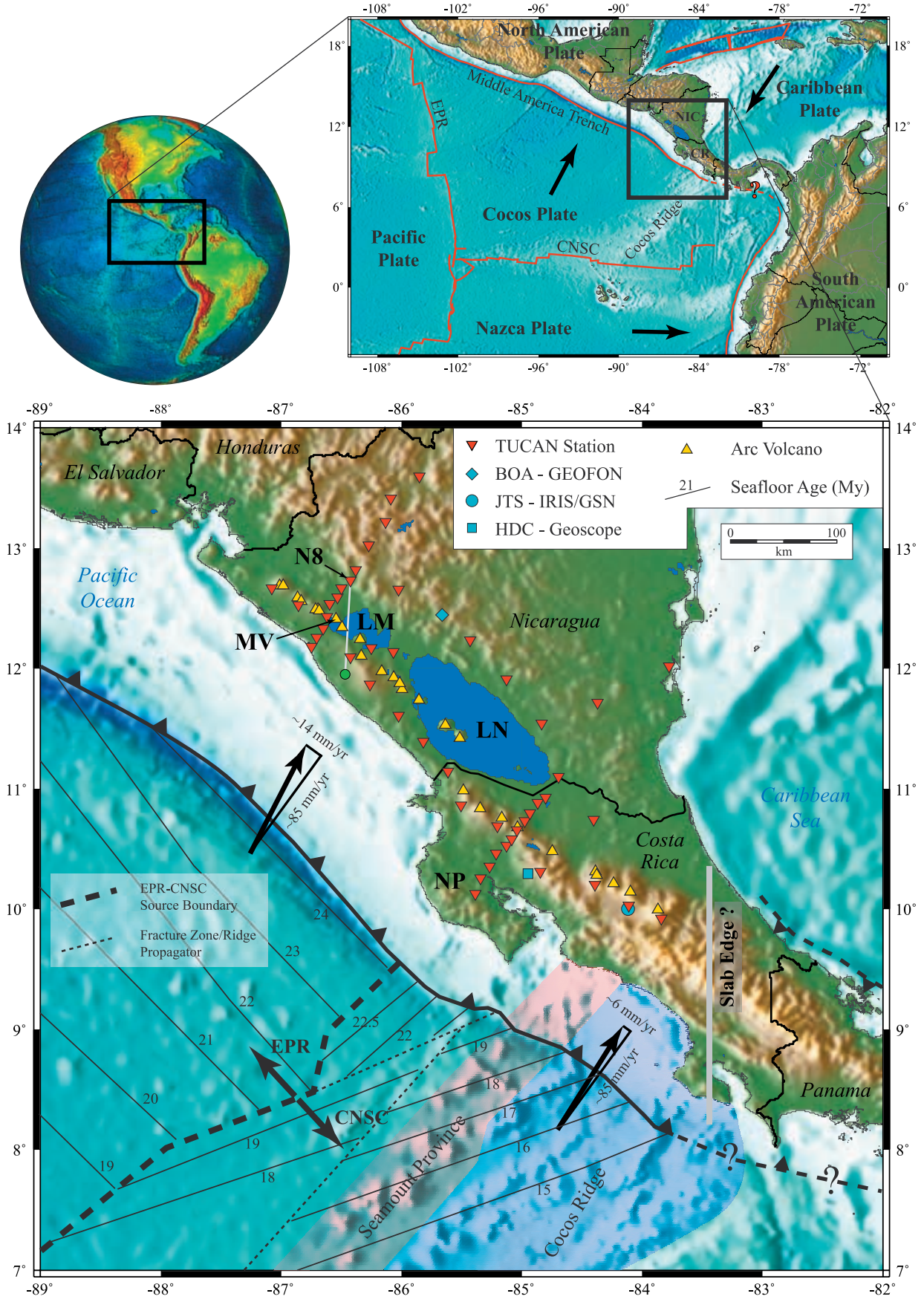

Figure 1

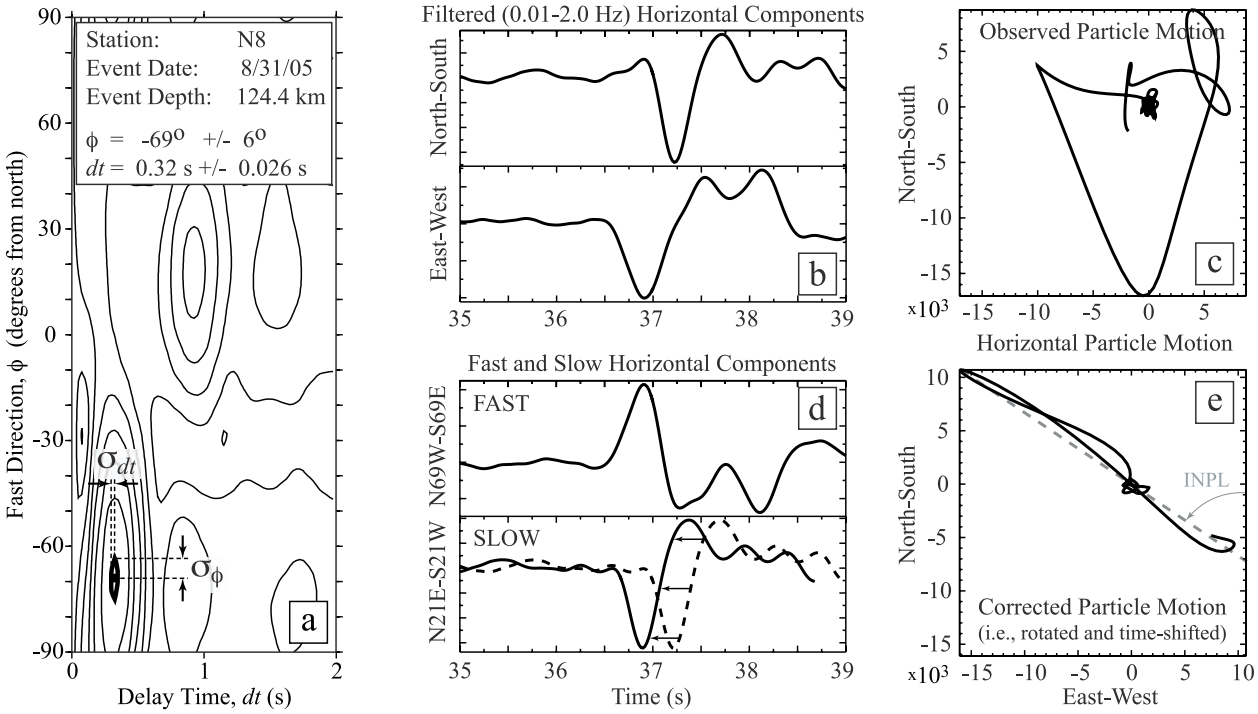

Figure 2. Example splitting measurement at TUCAN station N8 (see Figure 1). (a) Contoured values of the smaller eigenvalue in the cross-correlation matrix (λ_2) around the best fitting pair of splitting parameters (black dot, $\lambda_{2\min}$) (see section 3.1). The thick black ellipse encloses the 95% confidence region, and the maximum distances of this contour from the best fitting ϕ and dt values represent the respective uncertainties for these parameters (σ_ϕ and σ_{dt}). (b) Observed N and E components after applying a band-pass filter of 0.01–2.0 Hz. The offset of the phase on the two components is already visible. (c) Characteristic elliptical particle motion of the two horizontal components. (d) The top solid and dashed bottom waveforms are the result after rotating both components by ϕ (69° west of north), and then by time shifting the dashed wave by dt (0.32 s), the (e) corrected particle motion is obtained. The angle, INPL, of approximately linear particle motion is used as the initial polarization angle in the forward modeling discussed in section 4. Note that although we show only a 4 s window in Figures 2b and 2c, the actual window used in the calculation begins earlier.

waves to detect variations in anisotropic structure which SKS waves cannot. One downside to the local events used in this study is that they are generally small (magnitudes between 2.7 and 5.4), and therefore, the initial polarizations are unknown because source mechanisms are not readily available. This is in contrast to SKS waves, where upon conversion to a shear wave at the core-mantle boundary, all shear energy is in the radial direction, making the initial polarization parallel to the azimuth of the raypath.

3.1. Splitting Analysis Method

[13] We apply a band pass filter (0.01–2.0 Hz) to each waveform, a window 10–20 s before and ~1.5–2 periods after the S wave arrival is manually cut, and shear wave splitting parameters (i.e., fast horizontal S wave polarization azimuth, ϕ, and splitting time, dt) are calculated from the windowed waveform using the eigenvalue minimization method [*Silver and Chan*, 1991]. This technique attempts to linearize the horizontal components of particle motion by performing a grid search over all possible azimuths and a range of splitting times (Figure 2a); we use −90° to +90° at 1° increments for ϕ and 0 to 5 s at 0.01 s increments for dt. The horizontal components (Figure 2b) are rotated and time-shifted (Figure 2d) for each trial combination of splitting parameters, and a cross-correlation matrix is calculated. This matrix would possess only one nonzero eigenvalue if the resulting particle motion (corrected for splitting parameters) were to be perfectly linear, and the corresponding eigenvector would characterize the direction of linear particle motion. However, complexities can arise from background noise, lateral heterogeneities, and the possibility that the seismic wave being analyzed may have sampled multiple layers of anisotropy [e.g., *Silver and Savage*, 1994]. In practice, there will be two nonzero eigenvalues, and the

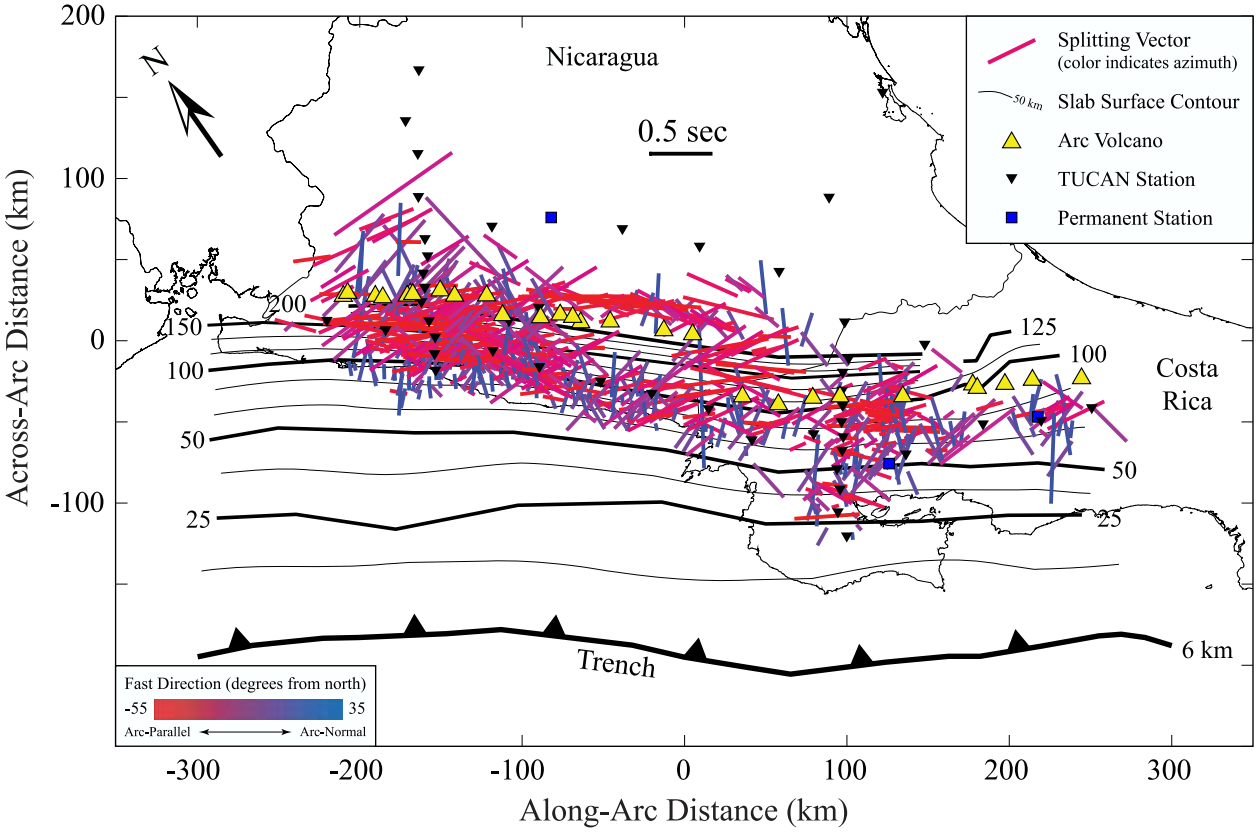

Figure 3. Shear wave splitting observations (colored vectors) from local events recorded at stations from the temporary TUCAN Broadband Seismic Experiment (inverted black triangles) and three permanent stations (blue squares). All 791 local S splits are plotted here at raypath midpoints, and because each is plotted at a different depth, many are obscured by overlying vectors. Length is scaled to splitting time (*dt*), and a reference vector for 0.5 s is shown (horizontal black vector in central Nicaragua). Vector orientation is parallel to fast direction (ϕ), with color grading between red (arc-parallel, N55°W) and blue (arc-normal, N35°E). This color scheme is used to help distinguish patterns so that regions showing significant coherence will stand out relative to those with many different orientations. For example, arc-parallel fast directions dominate along much of the Nicaraguan arc, as well as in the central Nicaraguan back arc, and this can be seen by the large proportion of red splitting vectors. Also note the relatively arc-normal orientation of most vectors beneath the Nicaraguan coast, where waves are predominantly sampling the wedge corner. However, there seem to be anomalies throughout the entire region, making it hard to interpret these measurements individually; thus the usefulness of a tomographic inversion becomes apparent. The coordinate system is rotated 35° east of north such that the approximate strike of the arc/trench is the x_1 direction and x_2 is arc-normal. Distances (used in the inversion) are in kilometers from (−85.5°, 11.5°), a rough approximation of the center of the array.

best fitting pair of splitting parameters is the one that minimizes the second eigenvalue [*Silver and Chan*, 1991] and produces the most linear particle motion (Figure 2e). Therefore, splitting parameters determined with this method are apparent splitting parameters that approximate the integrated effects of all anisotropic structure along the raypath. Errors (σ_ϕ and σ_{dt}) are measured on the 95% confidence contour at the maximum distance in the ϕ and *dt* directions, independently, from the best fitting pair of splitting parameters (Figure 2a).

3.2. Data Set

[14] Shear wave splitting was measured in local S phases recorded by the stations of the TUCAN Broadband Seismic Experiment. The TUCAN array was operational from July 2004 to March 2006 and consisted of 48 broadband stations that formed a fore arc, back arc, and two cross-arc lines (Figure 1), with station spacing varying between 10 km and 50 km. Splitting was also measured at three permanent stations: JTS (Global Seismograph Network, IRIS–Scripps Institution of Oceanography),

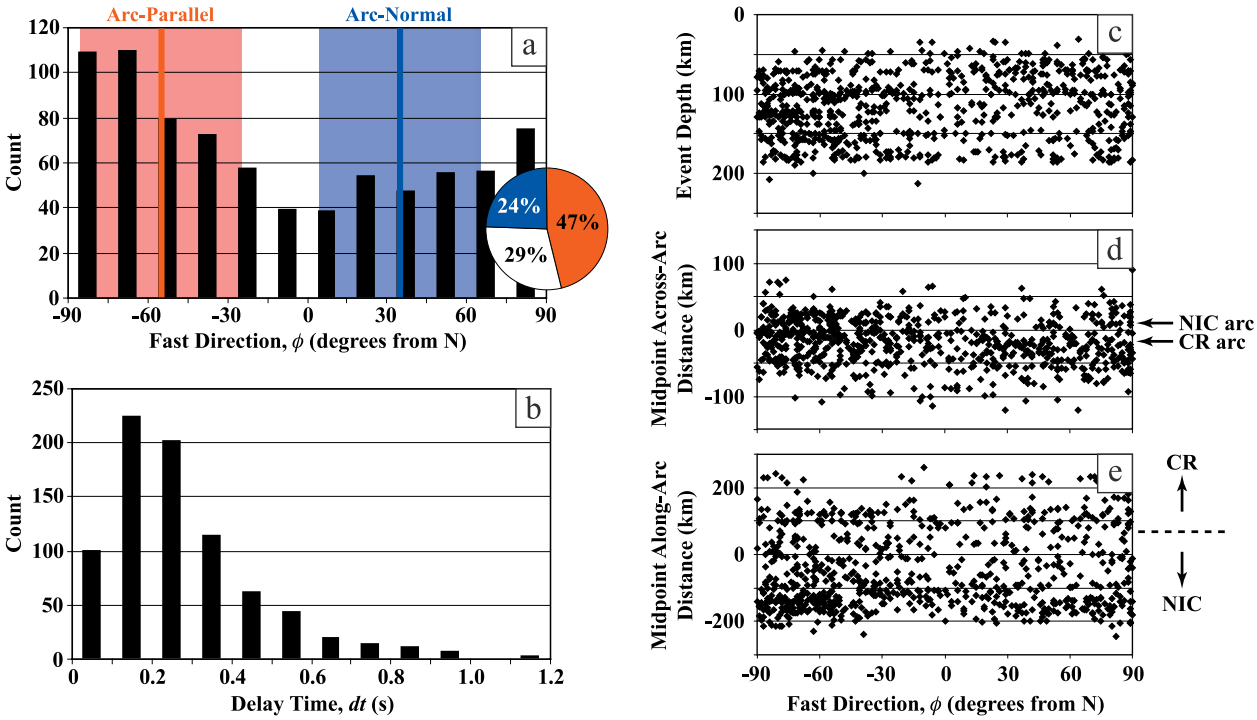

Figure 4. Shear wave splitting parameter statistics. (a) Histogram of ϕ in bins of 15°. The red and blue boxes denote a range of fast directions ±30° from arc-parallel and arc-normal, respectively. There is a predominance of approximately arc-parallel fast directions, but this data set is not bimodal (note pie chart, with blue denoting arc-normal, red denoting arc-parallel, and white denoting intermediate), as is seen in Japan [*Nakajima et al.*, 2006], and would be predicted with 2-D corner flow and B-type fabric in the wedge corner [e.g., *Kneller et al.*, 2005]. (b) Histogram of *dt* in bins of 0.1 s. (c) Fast direction versus event depth. (d) Fast direction plotted against the across-arc distance of the midpoint of each ray. (e) Fast direction versus along-arc distance of each midpoint. Figures 4c–4e demonstrate no clear correlation exists for the entire data set between location and fast direction.

HDC (GEOSCOPE, Institut de Physique du Globe de Paris), and BOA (GEOFON, Program of GFZ Potsdam). From ~20 months of data, we analyzed 8581 local S waveforms, resulting in 791 high-quality splitting measurements (Figure 3 and Table S1).[1] We do not define "high-quality" splits exclusively by the size of the 95% confidence region, but rather, each measurement is assessed on the basis of four attributes. A "high-quality" splitting measurement (1) is made from a clear phase with a high signal-to-noise ratio; (2) displays elliptical or circular particle motion; (3) has a small, single 95% contour (preferably enclosed by multiple contours); and (4) yields roughly linear particle motion when the waveform components are corrected for splitting. See Table S1 (auxiliary material) for a complete spreadsheet of event, station, and splitting parameter information.

[15] This data set is complex and shows a high degree of spatial variability in both ϕ and dt, not unlike other subduction zones [e.g., *Morley et al.*, 2006; *Pozgay et al.*, 2007]. There is no obvious simple correlation between event characteristics (e.g., depth, path length, across-arc/along-arc position) and splitting fast direction (Figure 4), making it difficult for any simple 1-D or 2-D model of anisotropy to account for all observations. At first glance, it may be tempting to attribute such a distribution to short-wavelength structural variations in the subducting or overriding crust/lithosphere. However, path segments through the subducting slab do not typically constitute a significant fraction of the total path length, and delay times show a clear increase with increasing path length when averaged in depth bins (Figure 5), indicating the presence of anisotropy in the mantle wedge beneath the overriding plate.

[16] Despite the complexity of the data set as a whole, sorting by depth and geographic location does reveal underlying structure in the measurements. In the northwest Nicaraguan fore arc, a transition from arc-normal fast directions in the extreme fore arc to arc-parallel fast directions

[1]Auxiliary materials are available in the HTML. doi:10.1029/2009GC002375.

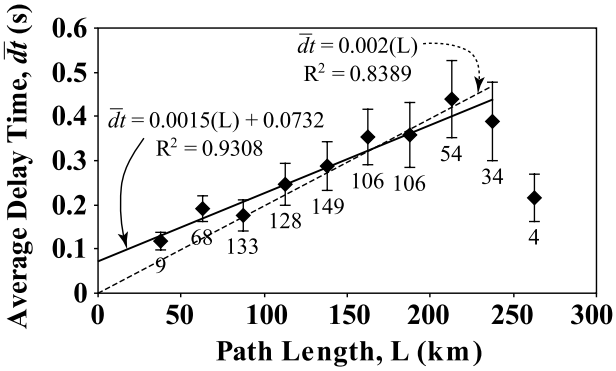

Figure 5. Average delay time for 25 km bins of straight-line path length. Error bars show the average 1σ for the average *dt* in each bin, and the numbers below each data point indicate the number of splits in each bin. The very coherent trend of increasing birefringence with increasing path length indicates that the mantle wedge is the dominant source of anisotropy. The solid line shows the best fit linear trend of the data (excluding the four longest paths), while the dashed line gives the trend assuming that delay time goes to zero as path length goes to zero. The disparity between these two trends may indicate the presence of anisotropy in the overriding lithosphere or crust that is strong relative to that in the mantle wedge but which occurs over such a small fraction of total path lengths that the mantle wedge anisotropy dominates.

toward the arc occurs (Figure 6a); this pattern becomes less apparent moving along the arc toward and into Costa Rica (Figure 3). Another example is in the Nicaraguan back arc where measured fast directions rotate from arc-parallel in central Nicaragua to more arc-normal in the northwest (Figure 6b). One of the challenges posed by a large, complicated shear wave splitting data set, such as this one in Central America, is finding a model of anisotropy that can account for short-wavelength variability and, sometimes, even contradictory splitting observations at similar locations. We therefore turn to tomography to produce a model of anisotropic structure that best explains the splitting observations.

4. Shear Wave Splitting Tomography

[17] If three-dimensionally heterogeneous anisotropic structure exists above the local S sources, then the large scatter of ϕ and *dt*, when plotted at a single point (e.g., hypocenter, raypath midpoint, station) is not surprising considering that raypaths with a common point may sample distinctly different structure outside the shared region and that ϕ and *dt* are dependent on path length and both propagation and polarization direction. The spatial averaging technique developed by *Audoine et al.* [2004], and later utilized by *Nakajima et al.* [2006] and *Pozgay et al.* [2007], begins to address the possibility of heterogeneous anisotropy in subduction zones by projecting individual splitting parameters to the surface, but does not incorporate the effects of multiple layers of anisotropy on predicted particle motions.

[18] The distribution of local seismic sources and receivers in Nicaragua–Costa Rica (Figure 7) and the large number of high-quality splitting measurements (Figure 3) provide the opportunity to employ the use of a formal inversion to resolve anisotropic structure in this subduction zone. A more detailed discussion and validation of this technique is described by *Abt and Fischer* [2008], but the principle assumptions regarding mantle composition, elastic properties, and Earth structure are restated here. Brief explanations of the forward modeling and inversion are also provided before presenting the modeling results.

4.1. Mineralogy

[19] A model mantle mineralogy of 70% olivine and 30% orthopyroxene (opx) was assumed, and we used the elastic constants of olivine ($Mg_{1.8}Fe_{0.2}SiO_4$) [*Anderson and Isaak*, 1995; *Abramson et al.*, 1997] and opx ($Mg_{0.8}Fe_{0.2}SiO_3$) [*Frisillo and Barsch*, 1972], including their pressure and temperature derivatives [see *Abt and Fischer*, 2008, Table 1]. Naturally deformed lithospheric peridotites [e.g., *Mainprice and Silver*, 1993] exhibit orthorhombic symmetry in both olivine and opx and a LPO in which the *a* axis [100] of olivine is aligned parallel to the *c* axis [001] of opx (*b* axis [010] of olivine is parallel to the *a* axis [100] of opx). Adding the stiffness tensors ($0.7*c_{ijkl}^{olivine} + 0.3*c_{ijkl}^{opx}$) in this orientation provides the elastic properties for our orthorhombic model mantle material.

[20] Although olivine and opx are intrinsically orthorhombic, several studies have demonstrated that crystal aggregates display hexagonal symmetry, rather than purely orthorhombic symmetry [*Mainprice and Silver*, 1993; *Bystricky et al.*, 2000; *Mehl et al.*, 2003; *Michibayashi et al.*, 2006]. For example, *Bystricky et al.* [2000] and *Michibayashi et al.* [2006] observe LPO in which olivine *a* axes are aligned ~parallel with the shear direction and the *b* and *c* axes form a "girdle" perpendicular to the shear direction (i.e., D-type slip, {0*kl*}[100]). In order to simulate hexagonal symmetry using the orthorhombic single-crystal

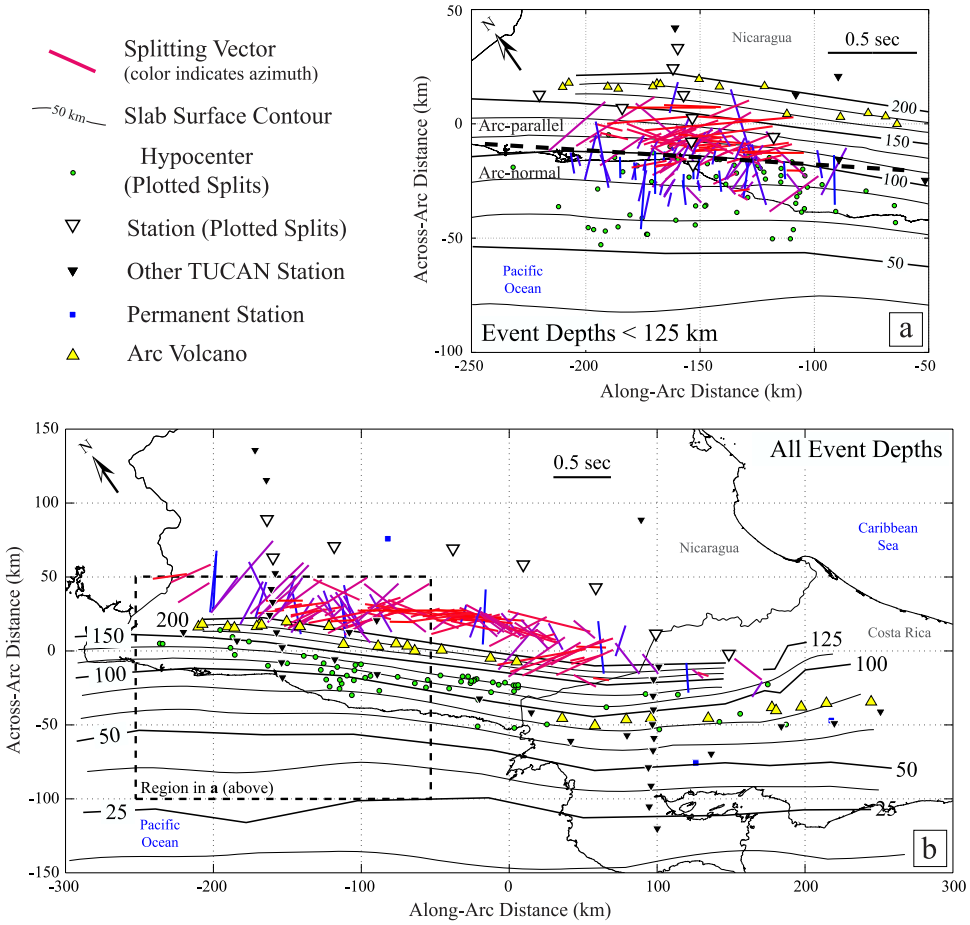

Figure 6. Subsets of the shear wave splitting measurements show greater coherence than the entire data set (Figure 3). The larger inverted empty black triangles represent the stations at which the splits shown were measured. (a) In NW Nicaragua, for splits from shallow events (<125 km), a relatively sharp transition (thick dashed line) occurs between arc-normal fast directions closer to the trench and arc-parallel fast directions toward the arc. This pattern is predicted for along-arc flow and B-type fabric in the cold wedge corner [*Jung and Karato*, 2001; *Kneller et al.*, 2005] but is the inverse of what would be expected for 2-D corner flow (i.e., arc-parallel fast directions close to the trench and changing to arc-normal in the arc and back arc). (b) Across the central Nicaraguan back-arc region, fast directions are strongly arc-parallel, while more oblique fast directions are observed to the NW and SE.

elastic constants of olivine and opx, the coefficients corresponding to the *b* and *c* axes must be combined. We prescribed the olivine *a* axis [100] (opx *c* axis [001]) as the axis of symmetry and reduced the nine independent orthorhombic coefficients to five independent hexagonal coefficients [*Montagner and Anderson*, 1989]. As discussed in section 4.4, here we only present models that assume this hexagonal symmetry.

[21] We made the simplifying assumption that the entire model is composed of the olivine-opx material described above and, therefore, do not account for crustal mineralogies or the elastic properties of cracks/fractures at crustal depths. A more realistic characterization of crustal anisotropy is one aspect of the modeling that could be addressed in the future to help isolate the effects of mantle wedge fabric.

4.2. Model Parameterization

[22] The model region (i.e., a volume encompassing all events and stations) was parameterized into blocks 25 km on each side (Figure 8). Crystallographic orientation in each model block was set by two (θ,ψ, hexagonal case) or three (θ,ψ,γ, orthorhombic case) angle parameters. θ represents the horizontal azimuth of the [100] axis, ψ is the plunge of the [100] axis from horizontal, and γ is the plunge of the [001] axis (Figure 8). We employed a scalar parameter, α, to allow for variable strength of anisotropy. This parameter varies from 0% to 100% and reduces the effect of anisotropy on predicted delay time in each model block relative to that from its single crystal value. Conceptually, α can represent a percentage

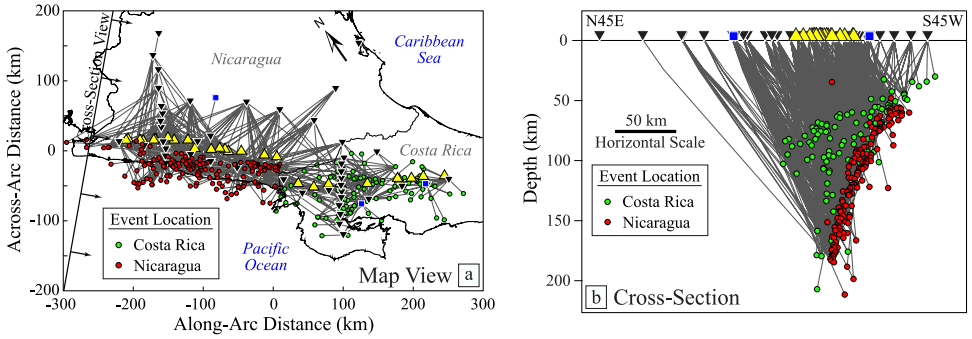

Figure 7. Event distribution and ray coverage in (a) map view and (b) cross section for the shear wave splitting data set used in the inversion. Note that although the model is parameterized as blocks in an along-arc (N55°W) and across-arc (N35°E) direction, the cross section here (Figure 7b) is shown oblique to this orientation (N45°E) because the strike of the slab changes slightly along the arc. Yellow triangles are volcanoes, black inverted triangles are TUCAN stations, and blue squares are permanent stations.

of randomly oriented grains mixed with grains aligned by the specified orientation parameters for a particular block.

4.3. Forward Calculation

[23] We calculated predicted shear wave splitting parameters (ϕ, dt) for each raypath in the data set (Figure 7) using a particle motion perturbation method [e.g., *Rümpker and Silver*, 1998; *Fischer et al.*, 2000]. The effects of three-dimensionally varying anisotropy on the horizontal components of shear wave particle motion were approximated by progressively rotating and time shifting a simple wavelet according to the eigenvectors (polarization directions) and eigenvalues (phase velocities) of the Christoffel matrix [*Babuska and Cara*, 1991] for each model block touched by a ray. (See *Abt and Fischer* [2008] for more details. Note the typographical error in the indices of *Abt and Fischer* [2008, equation 1]. The Christoffel equation should be $m_{ik} = 1/\rho(z)*c_{ijkl}*n_j*n_l$.) This technique accounts for the order in which anisotropic structure is encountered by a wave and is sufficiently efficient to allow for its repetitive use in calculating partial derivatives needed for the inversion. The particle motion perturbation approach does not consider Fresnel zones of the local S phases. However, a comparison [*Abt and Fischer*, 2008] of the splitting parameters calculated with this approach to those obtained from full-waveform

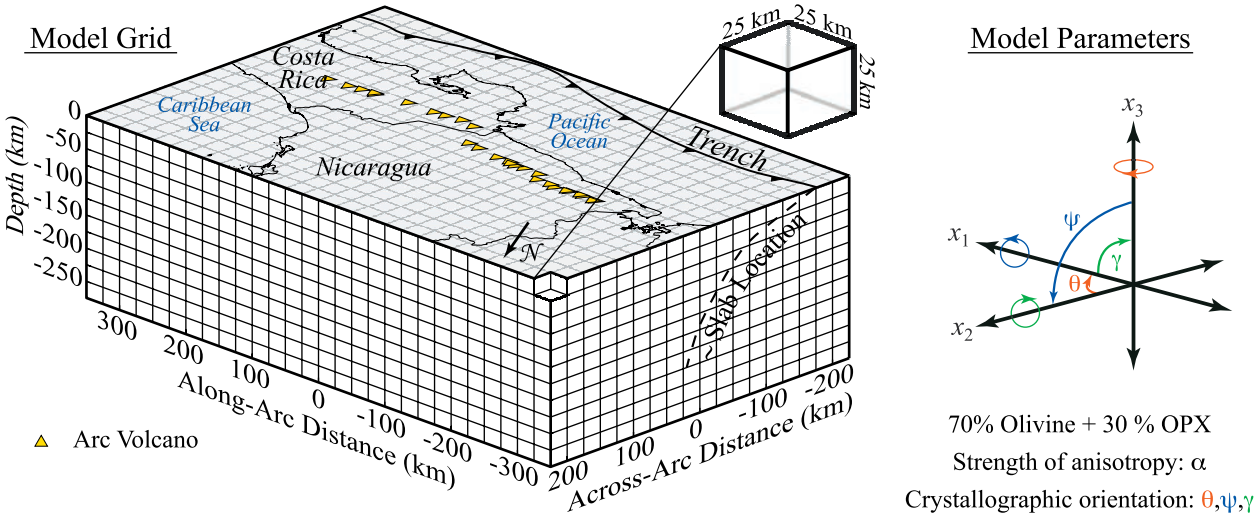

Figure 8. Model discretization and parameterization. (left) The elastic properties of olivine [*Anderson and Isaak*, 1995; *Abramson et al.*, 1997] and orthopyroxene [*Frisillo and Barsch*, 1972] are assigned to each model block, (right) with their orientation defined by rotation angles. For the hexagonal symmetry approximation, only two angles (θ and ψ) are needed. The strength of fabric alignment is determined by the scalar parameter α. The grid of model blocks is shown relative to the volcanic arc (yellow triangles), Nicaragua–Costa Rica coastline, trench, and approximate location of the subducting Cocos Plate at depth beneath northwest Nicaragua.

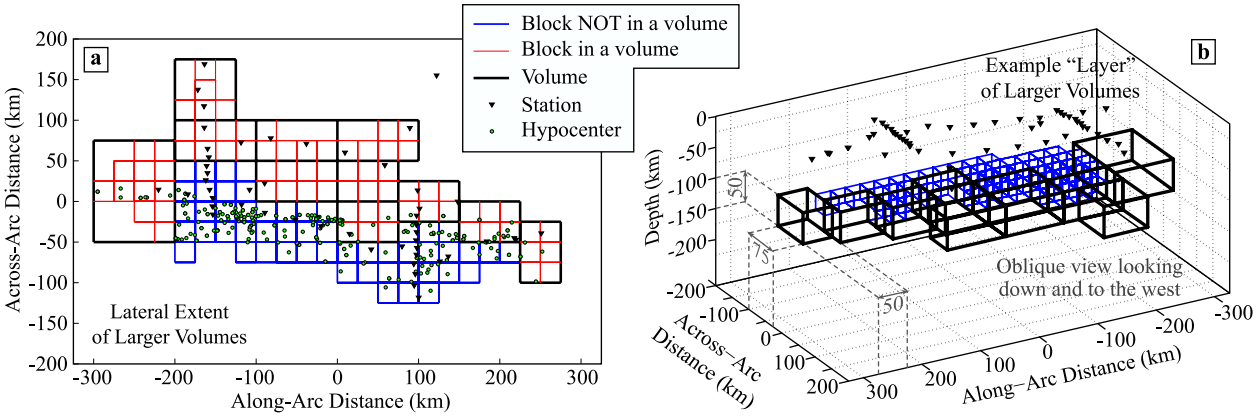

Figure 9. Larger volumes generated to increase resolution of individual parameters and expand the interpretable region of the model space. Blue blocks are those that remain independent after volumes (thick black lines) are formed. (a) Lateral extent of volumes. The red blocks are those within the volume that are actually touched by a ray and used in the inversion. (b) Example "layer" of larger volumes and independent blocks. The lateral extent of each larger volume does not change with depth, and each layer is 50 km thick, except for the surface layer, which is only 25 km. For clarity, the red blocks within the volumes are not shown here.

pseudospectral synthetics [*Hung and Forsyth*, 1998] for moderately large variations in anisotropy showed they were in close enough agreement that any inaccuracy in predicted splitting parameters introduced by the particle motion perturbation method will likely be much smaller than the uncertainties typical of the observed shear wave splitting parameters inverted in this study.

4.4. Inversion

[24] A best fitting model of anisotropy (i.e., crystallographic orientation and strength of fabric alignment) was determined by minimizing the misfit between observed and predicted shear wave splitting parameters through an iterative, damped, linearized, least squares inversion [*Tarantola*, 1987]. The effects of model parameter changes ($\delta\theta$, $\delta\psi$, $\delta\gamma$, $\delta\alpha$) on predicted splitting parameters ($\delta\phi$, δdt) were calculated numerically by simple finite difference. However, to account for nonlinearities in the dependence of splitting on model parameters, we recalculate partial derivatives when model parameters changed by more than 1° (for θ, ψ, γ) or 1% (for α).

[25] The data were weighted by their individual errors (section 3.1 and Table S1) and the inversion was damped in order to keep changes in model parameters small enough such that the linear partial derivatives used in each iteration are valid. The a priori variance was increased (i.e., damping was decreased) after initial model convergence to test the stability of the model. On the basis of tests of inversion accuracy with synthetic data [*Abt and Fischer*, 2008], inversions were run for a total of 100 iterations, with variance increased from 1 (degrees or %) to 10 after iteration 40. The event and station distribution in the current data set is such that regions of the back arc contain fewer crossing rays than beneath the arc and fore arc (Figure 7), resulting in reduced resolution in the back arc. To allow modeled crystallographic orientations to be interpreted, at a coarser resolution, in larger portions of the back arc, we combined multiple individual 25^3 km^3 blocks into larger effective volumes following convergence of the model after damping relaxation. The extent of these larger volumes is shown in Figure 9, and their incorporation into the inversion was accomplished by averaging crystallographic orientation and strength of anisotropy in each block within a volume and then introducing constraints into the inversion that forced subsequent model parameter changes in blocks within a volume to be the same. This approach is described in more detail by *Abt and Fischer* [2008]. The large volume constraints were emplaced after iteration 70 with an associated variance value of 0.1. This variance value controls the degree to which the individual blocks within a volume are forced to maintain the same parameters (i.e., act as one coherent block). Relative to the splitting data variances, which are the errors from the splitting measurements, a value of 0.1 is sufficiently small for the large volume constraints to dominate over any change in the model parameters for an individual block that would otherwise be required by trying to match the observed splitting parameters alone.

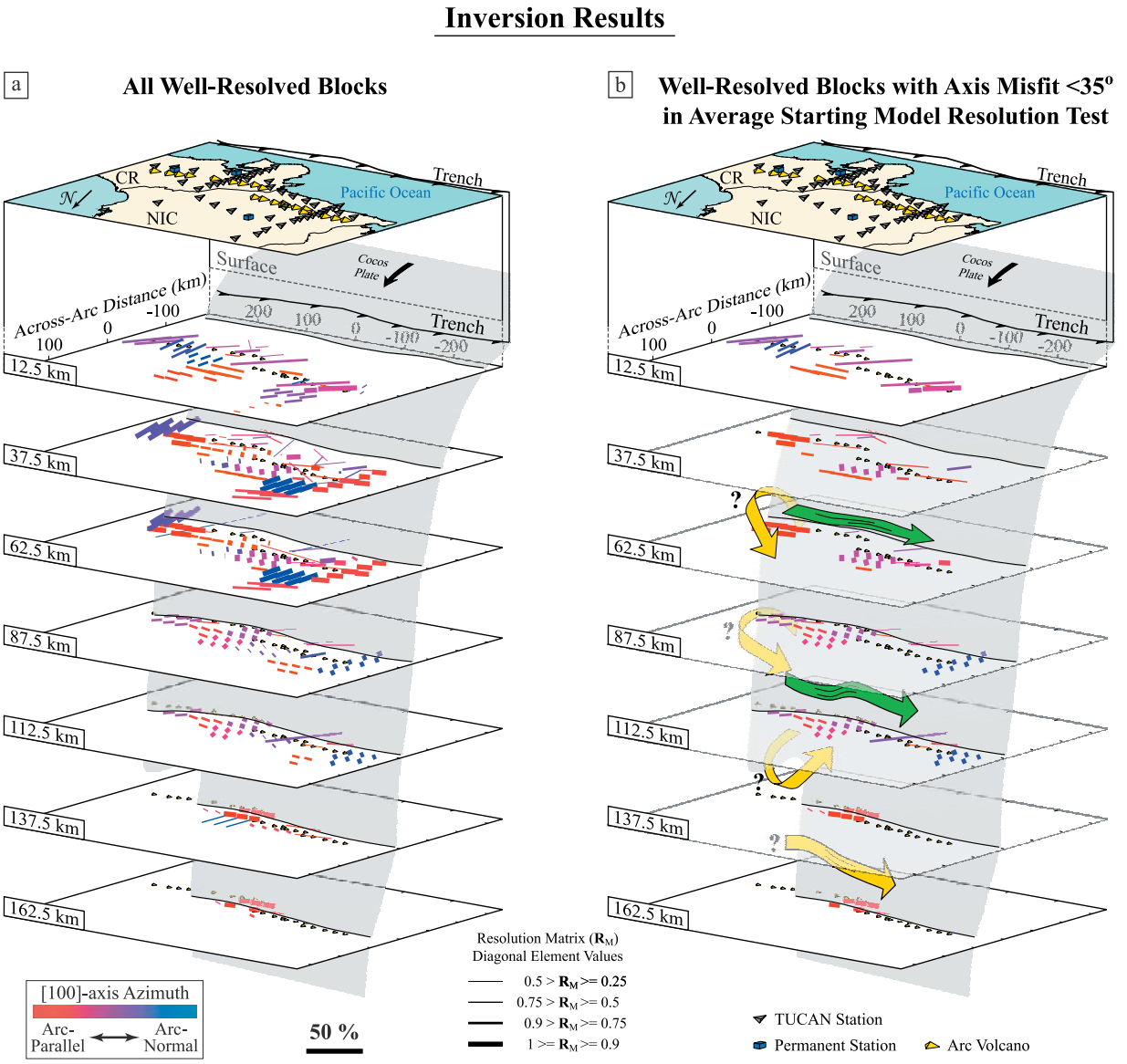

Figure 10. Model of anisotropy in the mantle wedge beneath Costa Rica and Nicaragua. Vectors represent *a* axes of olivine, and although dip is solved for, the axes have been projected onto horizontal planes to emphasize their azimuthal orientation. Color represents azimuth and varies from arc-parallel (red) to arc-normal (blue). The thickness of model vectors (here and in Figures 11, 13, and 14a) is scaled by the resolution matrix diagonal element values; qualitatively, thicker vectors are better resolved, and thinner vectors are less well resolved. The intersection of the Cocos Plate (gray surface) with each cross section is shown with a black line (i.e., slab contours), and the volcanic arc is shown for reference on each cross section as well (small yellow triangles). (a) Model blocks deemed "well resolved" from the resolution matrix, with the thickness of each vector corresponding to the associated resolution matrix diagonal element value (e.g., thinnest lines > = 0.25, thickest lines > = 0.90). (b) Model blocks from Figure 10a that also have *a* axis angular misfits < = 35° between the input and retrieved structure in the recovery test using the average starting model (Figure 14b). These remaining vectors are those which we most confidently interpret. Owing to their location in the mantle wedge (see section 5.2), we interpret the roughly arc-parallel orientation of most *a* axes to indicate the presence of arc-parallel directed shear (i.e., flow) in the mantle wedge. Yellow arrows around the edge of the slab indicate possible flow paths, while horizontal green arrows show the dominant orientation of flow suggested by both shear wave splitting tomography and geochemical trends (section 5.3). Our current data and inversion do not distinguish between flow with a horizontal shear plane and that with a vertical shear plane (i.e., that observed in the exposed Talkeetna arc in Alaska [*Mehl et al.*, 2003]), and therefore we illustrate both as possibilities.

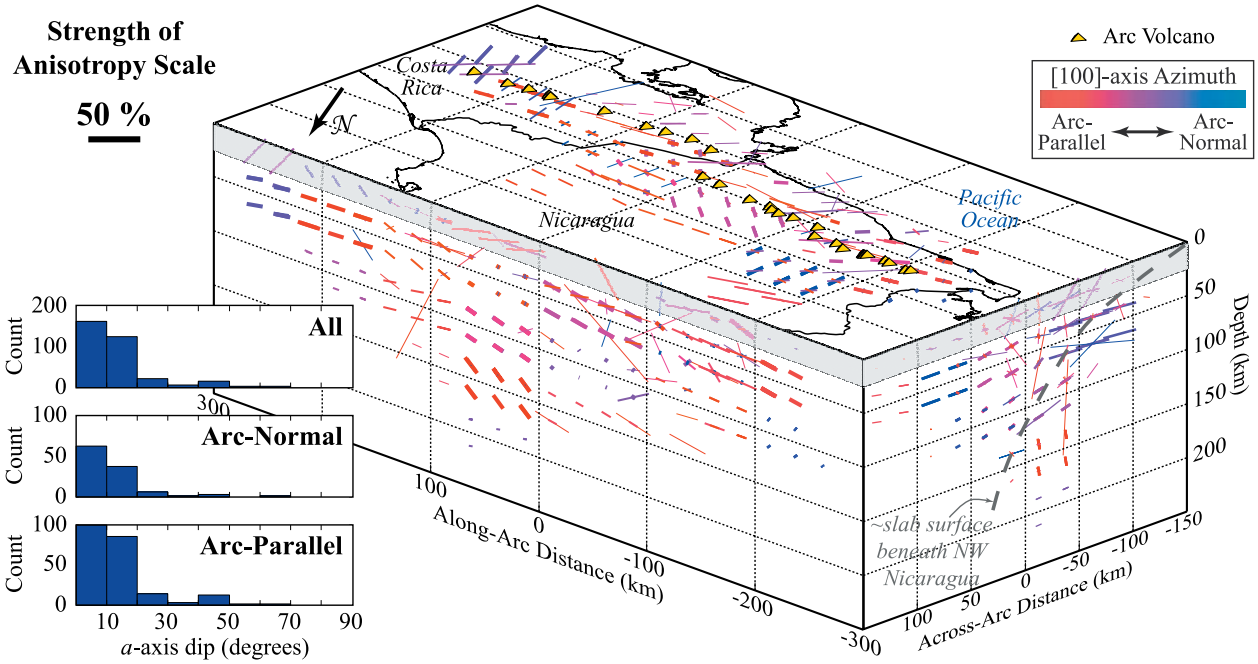

Figure 11. Pseudo-3-D view of the model of anisotropy shown in Figure 10. All well-resolved model *a* axes (as determined by the resolution matrix) are projected onto an along-arc, an across-arc, and a horizontal plane. The dip of arc-parallel (arc-normal) *a* axes can be seen in the along-arc (across-arc) cross section. The most prominent deviations in *a* axes from horizontal are found in the fore-arc wedge beneath Nicaragua between −50 and −200 km in the along-arc direction. However, histograms of *a* axis dip are shown to the left, and nearly all well-resolved *a* axes have dips less than 20°. The gray masking of the top layer is meant as a reminder that the mineralogy, and thus anisotropy, at crustal depths is likely not directly interpretable.

[26] Although we conducted inversions with all four model parameters (α, θ, ψ, γ) assuming orthorhombic symmetry, we found that γ, the parameter controlling *c* axis dip, is less well resolved than the other two angle parameters. Furthermore, there are only minor differences in the predicted splitting parameters between an LPO with hexagonal symmetry and orthorhombic symmetry with the *c* axis fixed in the horizontal plane ($\gamma = 0$). Therefore, we present results from inversions that assumed hexagonal symmetry and solved for three parameters: fabric strength (α) and the azimuth (θ) and dip (ψ) of the symmetry axis (i.e., the olivine *a* axis).

[27] An "average" starting model was used for the inversion of the real data. This model was generated by setting θ in each block to be the average fast direction of all rays that touch that particular block and by setting $\psi = 0$ (i.e., horizontal *a* axis) and α to be that predicted from the average delay times of all rays that touch that particular block. (See *Abt and Fischer* [2008, Appendix A] for a full description.) The starting model assumed does affect the inversion results, but during testing of the tomographic method with synthetic data we found that inversions with the average starting model, used in concert with the inversion parameter values given above, retrieve synthetic known structures with the greatest accuracy [*Abt and Fischer*, 2008].

4.5. Tomographic Modeling Results

[28] The final model of crystallographic orientation obtained from the inversion is first shown in Figure 10. Model parameter resolution was determined with the resolution matrix [*Tarantola*, 1987], and in Figure 10a we show results for model blocks which have resolution matrix diagonal element values greater than 0.25 for all model parameters. In this view, the *a* axes of olivine are projected onto horizontal planes, thereby showing azimuthal orientation but not dip. Arc-parallel and nearly arc-parallel *a* axes dominate a significant portion of the model space. Three separate "pockets" of arc-normal *a* axes exist, but as demonstrated in section 4.6, they are not all uniquely resolved. The dips of olivine *a* axes are revealed in a pseudo-3-D view of the model (Figure 11). In general, *a* axes (arc-parallel, arc-normal, and intermediate) are close to horizontal, with only a slight tendency toward

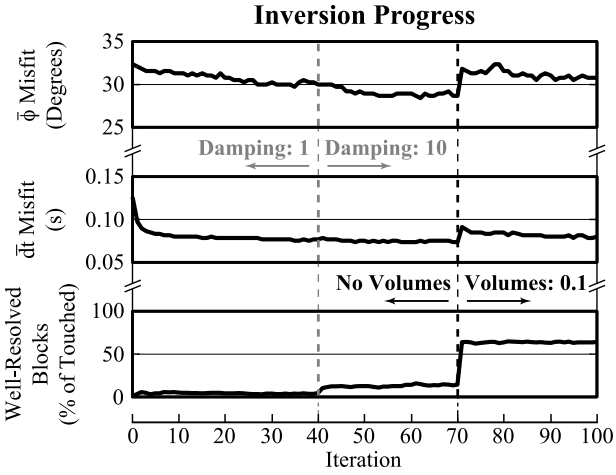

Figure 12. Progression of data misfit during the inversion. Average fast direction misfit and average delay time misfit are weighted by errors in both the splitting observations and the calculation of synthetic splitting parameters. The relaxation in damping at iteration 40 does not result in any observable instability in the model (i.e., a dramatic change in the model leading to a commensurate increase or decrease in data misfit). The resolution matrix takes into account the level of damping, and therefore, increasing a priori variance (i.e., reducing the penalty function constraints) leads to a slight increase in the number of "well-resolved" blocks. When blocks are grouped into volumes at iteration 70, the model parameters in each block within a volume are averaged, resulting in a spike in misfit. However, acting as one larger block allows for a greater number of raypaths to constrain the best fitting LPO, and therefore a much larger portion of the model space becomes interpretable.

dipping to the north-northwest. As demonstrated by *Abt and Fischer* [2008], *a* axis dip is partially resolvable, particularly beneath the two arc-normal station lines where crossing ray coverage is most dense. Therefore, along with the dominantly arc-parallel *a* axis azimuths, the overall roughly horizontal orientation of *a* axes displayed in Figure 11 is also a significant feature of the model. The accuracy of *a* axis azimuth and dip recovery is discussed further in section 4.6.

[29] Over the course of the inversion, both average fast direction misfit and delay time misfit decrease relatively smoothly until reaching the point where the model discretization is effectively coarsened in the back arc, with no indication of instability caused by the relaxation of damping (Figure 12). When the larger volumes are first added to the inversion (iteration 70), the model parameters from the individual blocks contained in a single larger volume are averaged, resulting in a jump in average data misfit. As the inversion progresses, average delay time misfit returns to the same level (∼0.08 s), while average fast direction misfit retains a slightly higher value than before the volumes were generated (∼31° versus ∼29°). In the final model, the 95% confidence limits for the observed and predicted fast directions either overlap or are mismatched by less than 8° for 50% of the data, with mismatches of less than 28° for 75% of the data. Relative to their corresponding starting values, the final fast direction confidence limit mismatches represent a reduction of 22% for 50% of the data and 8% for 75% of the data. The 95% confidence limits for the observed and predicted times either overlap or are mismatched by less than 0.01 s for 50% of the data, and by less than 0.07 s for 75% of the data; these values represent 85% and 52% reductions from starting values, respectively.

4.6. Recovery Tests

[30] We tested the uniqueness of our model (Figures 10 and 11) by conducting two recovery tests in which this model is used as a "known" input model of anisotropy. In conjunction with the characterization of resolution from the resolution matrix, comparing the recovered structure from these inversions with the "known" model allowed us to better define the location(s) in the model space that are particularly well constrained. Additional tests using simple input structures and synthetic data for the paths in the TUCAN data set were carried out by *Abt and Fischer* [2008]. They found that structures with lateral scales of 50–75 km are at least partially recovered down to depths of 100 km, particularly in the portions of the model space with the densest crossing ray coverage near the two arc-normal lines. At greater depths and at horizontal distances of more than 50 km into the back arc, spatial resolution rapidly decreases, particularly where the larger volume constraints are imposed.

[31] The first recovery test uses an average starting model, generated from the predicted splitting parameters in the same fashion as with the real data, and the inversion is run with the same parameters as the real data inversion (i.e., iterations, damping relaxation, larger volumes generated). In the work by *Abt and Fischer* [2008], resolution testing with synthetic models showed that input models were typically best retrieved when average starting models such as this one were employed. The final model from this recovery test is displayed in Figure 13a as the pseudo-3-D view and in Figure 14a

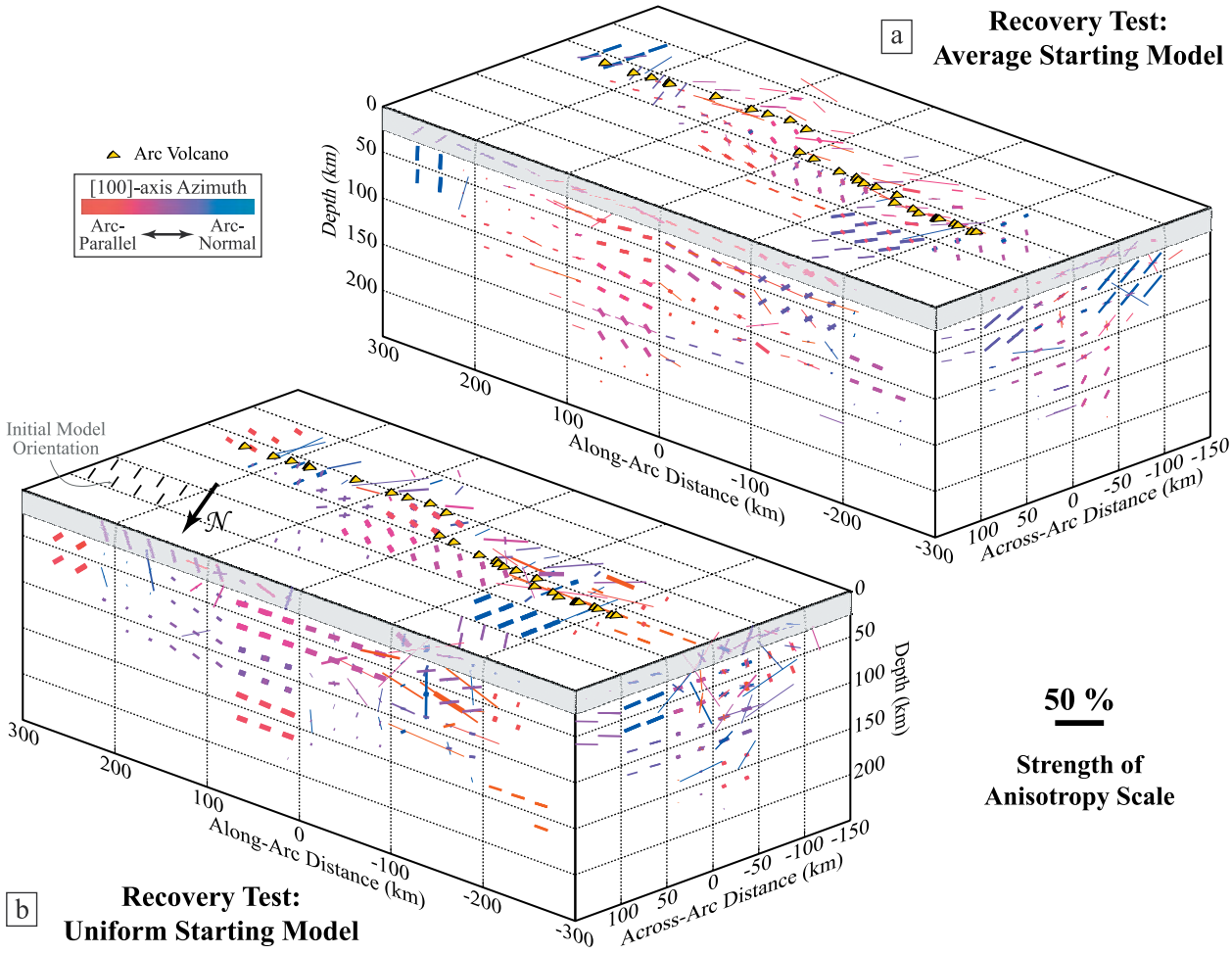

Figure 13. Recovery test results. All blocks shown are those considered well resolved by the resolution matrix from the final iteration of the inversion. (a) Final model from the recovery test using the average starting model. (b) Final model from the recovery test using the uniform starting model. The uniform starting model contained horizontal *a* axes oriented N-S with a strength of 25% (see eastern corner of the map view cross section). Note that because the resolution matrix is model-dependent, some model blocks that are considered well resolved in the real inversion (Figure 11) are not well resolved in the recovery test, and thus, vectors plotted in Figures 13a and 13b may not be plotted in Figure 11 and vice versa. Despite the dramatic difference in starting model, the large-scale structure in both recovery tests shows strong agreement with the input structure (i.e., predominantly arc-parallel *a* axes, with pockets of roughly arc-normal *a* axes beneath northwest Nicaragua and central Costa Rica).

with the *a* axes projected onto horizontal planes. Overall, the patterns of *a* axis orientation in the input model and the retrieved structure are similar, although a few blocks show large differences. In particular, *a* axis orientation is accurately recovered in much of the mantle wedge, as shown by the yellow and green regions in Figure 14b, which indicate angular misfits of less than 35° between input and retrieved model *a* axis orientation. Angular misfits include both azimuth and dip variations of *a* axes. In some regions angular misfit is large (>50°, red blocks in Figure 14b). These zones occur where crossing ray coverage is sparser, for example at the edges of the study region and in the middle of the array far from the two arc-normal lines of stations. The misfit in strength of anisotropy is less than 10% over most of the model (Figure 14c).

[32] The second recovery test is identical to the first except for the use of a uniform starting model in which *a* axes are horizontal and oriented N-S. The retrieved model from this recovery test is shown in Figure 13b, and the starting orientation is plotted for reference in the eastern corner of the map view cross section. As with the average starting model, retrieval of the input model is less accurate in more poorly sampled regions (e.g., the edges of the array and in between the arc-normal lines). The distribution and magnitude of angular

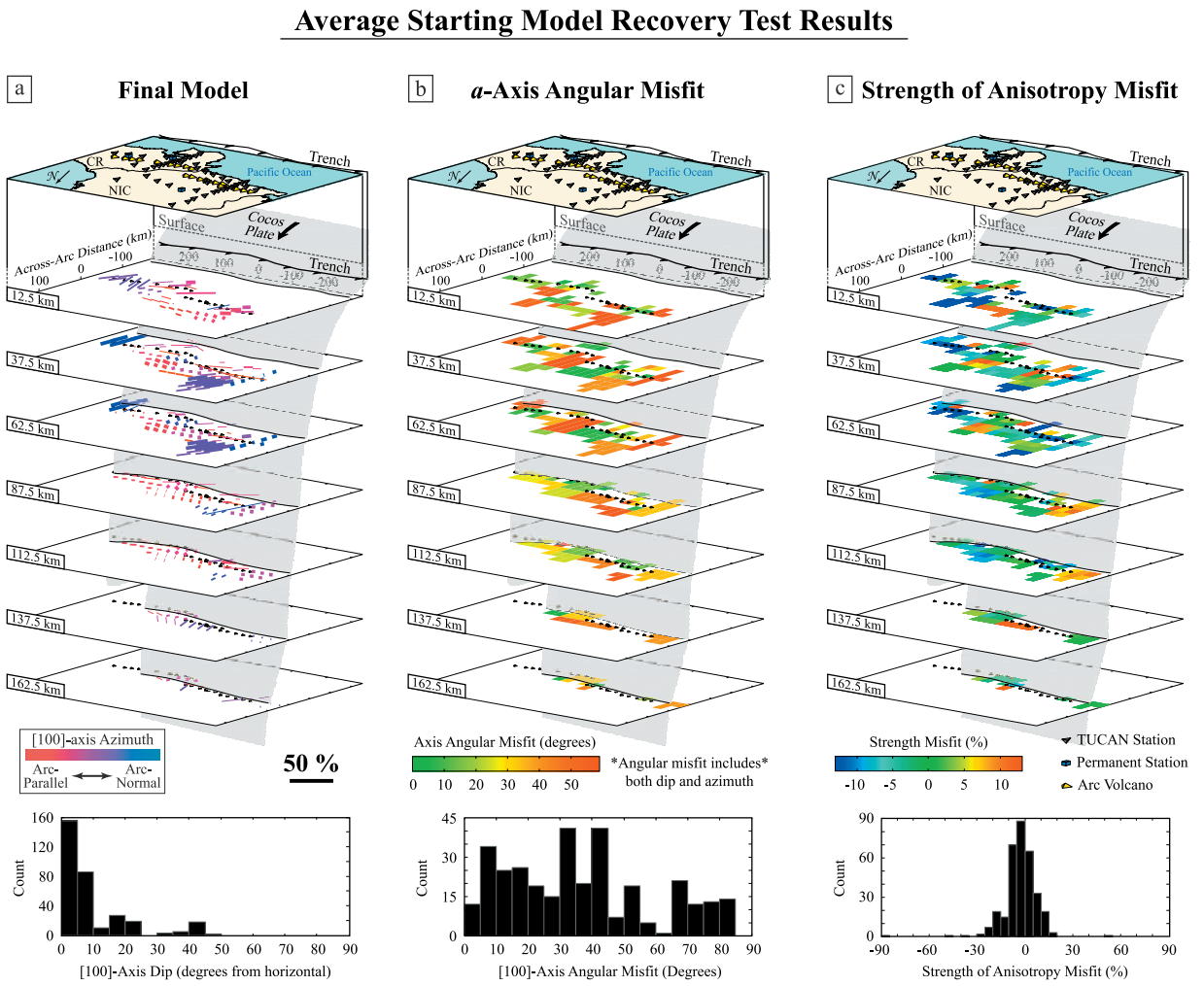

Figure 14. Recovery test results using an average starting model. (a) Same model as in Figure 13a except with *a* axes projected onto horizontal cross sections (for comparison with Figure 10a). As in Figure 13, only *a* axes in well resolved model blocks are shown. (b) Angular misfit between *a* axes in Figure 14a and those in Figure 10a. Angular misfit includes both dip and azimuth of the *a* axis. Azimuthal misfits are only slightly lower than angular misfits given the relatively horizontal orientation of most *a* axes (histogram below Figure 14a and Figure 11). The color scale has been saturated at one standard deviation from the mean in order to allow for variation at smaller misfits (<35°) to be distinguished; as shown by the histogram of axis misfits, this saturation affects ~50 blocks. (c) Strength of anisotropy misfit (negative values indicate a lower recovered strength). The color scale is again saturated at one standard deviation from the mean, but here the distribution is much narrower and fewer blocks fall outside this value.

misfit in this test (not shown) differs somewhat from the recovery test with the average starting model, particularly in poorly sampled regions, because of the fact that the average starting model is initially closer to the input structure. However, where sampling of the model space is good, the inversion with the uniform starting model also converges toward the input structure with no apparent tendency toward the starting orientation (Figure 13b). This inversion behavior indicates significant sensitivity of shear wave splitting to the model parameters, despite the nonlinear aspects of the forward calculation.

[33] At broad scales (hundreds of kilometers) within the better sampled regions, the results of the two recovery tests (Figures 13 and 14) and the known structure (Figures 10 and 11) agree fairly well. Most notably, the arc-parallel and sub-arc-parallel orientations of *a* axes beneath the arc and in the central portion of the back-arc mantle wedge beneath 75 km are consistently imaged. In addition, the pocket of roughly arc-normal *a* axes in northwest Nicaragua between 25 and 75 km depth is a stable feature in the models (Figure 13). The inversion with the average starting model retrieves the input structure somewhat more accurately be-

cause its initial deviations from the input structure are less extreme, a finding that agrees with the resolution testing conducted by *Abt and Fischer* [2008].

[34] Azimuths of olivine *a* axes are in general better resolved than *a* axis dips. For a single shear wave on a vertical path, similar splitting parameters may be predicted by a steeply dipping *a* axis with a large anisotropic strength and a horizontal *a* axis and a smaller strength. However, where phases sample a block over a wide range of back azimuths and incidence angles, this nonuniqueness is at least partially mitigated. *Abt and Fischer* [2008] showed that *a* axes with a 30° dip could be distinguished from a horizontal orientation down to depths of 75 km over broad regions of the fore arc and arc, and at least 75 km into the back arc. At greater depths, this accuracy of dip retrieval was limited to blocks beneath the intersection of the arc-parallel and arc-normal lines of stations. In the recovery tests shown in Figures 13 and 14, the accuracy of *a* axis dip retrieval varies significantly, but is better than 35° over significant regions of the model space (see Figure 14b, which shows the combined recovery of *a* axis dip and azimuth). In the model obtained by real data inversion (inset to Figure 11) and its recovery test using the average starting model (inset to Figure 14a) the majority of *a* axis dips are within 20° of horizontal. Therefore, in an overall sense we conclude that anisotropy resolved in the Nicaragua–Costa Rica mantle wedge can be characterized by a roughly horizontal fast symmetry axis.

[35] Because *a* axis dips in general are fairly small, we focus our interpretation on broad, well-resolved azimuthal patterns, in particular, differences between roughly arc-parallel or arc-normal *a* axis azimuths in better sampled model regions. To delineate the portions of the model space which are most robust and therefore interpretable, we chose regions where resolution matrix diagonal element values from our final model are greater than 0.25 (Figure 10a) and axis misfit between this model and the model from the recovery test with the average starting model is less than 35° (Figure 14). Even with this strict filter, roughly arc-parallel *a* axes are still apparent in the mantle wedge beneath the arc and back arc to depths of at least 125 km (Figure 10b). The pocket of arc-normal *a* axes beneath northwest Nicaragua between 25 and 75 km depth observed in the data inversion is replicated in the recovery tests with an azimuth misfit of 35°, but because of a modest discrepancy in dip, *a* axes in this pocket have total angular misfits of ~45° with the input structure and are therefore left out of Figure 10b. Additionally, there is a strong similarity between these large-scale structures (dominantly arc-parallel *a* axes and the arc-normal pocket) in the model and the pattern of observed splitting parameters (Figures 3 and 6).

[36] Some studies [e.g., *Faccenda et al.*, 2008] have proposed that the subducting slab is strongly anisotropic and that slab anisotropy dominates SKS splitting in subduction zones. In the tomographic models obtained in this study from local S splitting, slab anisotropy would be folded into the model blocks that lie below or contain the slab surface inferred from relocated hypocenters [*Syracuse et al.*, 2008]. Anisotropy within the slab is not in general clearly constrained, as demonstrated by the lack of "slab" blocks with well-resolved model parameters in Figures 10 and 14. This result is explained by the fact that most local S paths in the slab are fairly short, but it also indicates that the strength and geometry of slab anisotropy are such that they do not make a large overall contribution to the local S splitting. This finding echoes the correlation of splitting time with wedge path length (Figure 5), which in an average sense also shows that the local S splitting is dominated by wedge anisotropy.

5. Discussion

5.1. Interpreting Upper Mantle Deformation From Anisotropy Models

[37] The primary goal of this study is to place constraints on the pattern of flow in the mantle wedge beneath Nicaragua and Costa Rica using the model of anisotropy obtained by inverting local S shear wave splitting observations. The main features of this model are roughly horizontal and arc-parallel olivine *a* axes in the mantle wedge, with the suggestion of a zone of arc-normal *a* axes beneath northwest Nicaragua (Figure 10). The direction of shear can only be inferred from modeled *a* axis orientations if a relationship between the two is assumed (e.g., A-type slip, where olivine *a* axes align parallel to shear), but this relationship may not necessarily remain constant as conditions (e.g., pressure, temperature, melt, water) in the mantle wedge change. Along with the standard shear-parallel *a* axis interpretation [e.g., *Zhang and Karato*, 1995; *Ismaïl and Mainprice*, 1998; *Bystricky et al.*, 2000] we consider both B-type fabric [*Jung and Karato*, 2001; *Jung et al.*, 2006] and melt band formation [*Holtzman et al.*, 2003] as

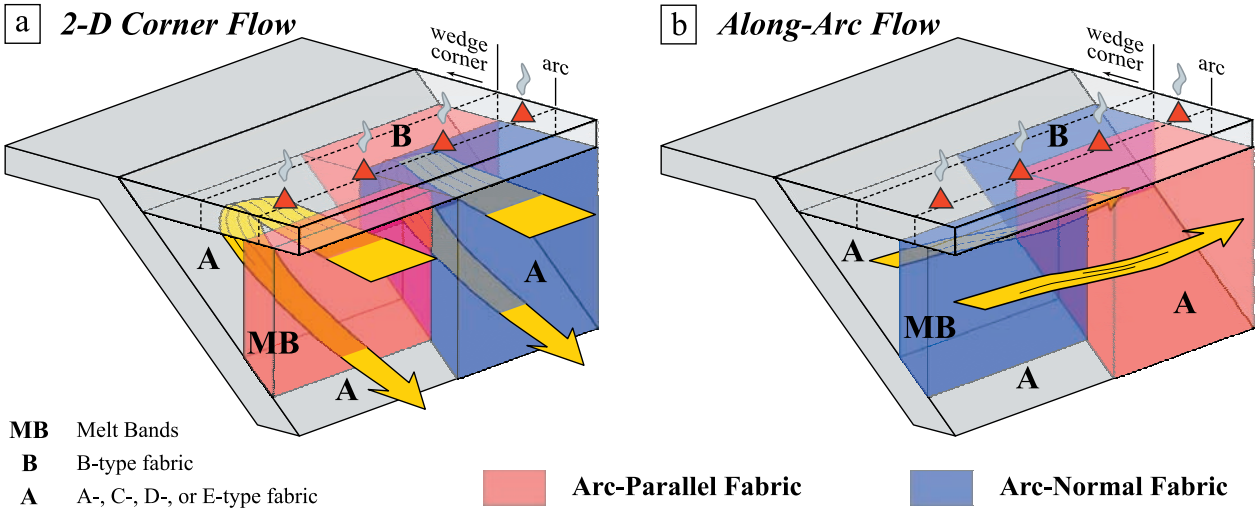

Figure 15. Interpreting the orientation of fast S wave polarization directions in terms of fabric generated by dislocation creep in olivine during simple shear in the upper mantle. Numerous studies of naturally and experimentally deformed polycrystalline peridotite (and olivine) show that the easiest (i.e., dominant) slip system in olivine will change as stress and water content (H/Si) increase. Despite the various combinations of crystallographic axis orientations relative to the shear plane and shear plane-normal, only the B-type fabric will result in the fast shear wave polarization direction (for a vertically propagating wave) being normal to the shear direction. Although the dominant slip system observed by *Holtzman et al.* [2003] is A-type, (010)[100], in the solid crystal lenses between melt bands, the fast seismic direction from both LPO and the melt bands themselves is normal to the shear direction. (a) Predicted fabric (i.e., fast shear wave polarization direction) orientation for 2-D corner flow in the presence of melt bands (MB, left side) or B-type fabric (B, right side). (b) Predicted fabric generated by predominantly along-arc flow in the presence of melt bands (MB, left side) or B-type fabric (B, right side). Note the location of expected deviations from A-type fabric (A) in the wedge relative to the arc and trench (dashed lines). Although predicted splitting parameters (especially ϕ) will vary somewhat across these boundaries, the pattern should mimic the underlying mantle fabric transitions [*Abt and Fischer*, 2008].

possible deviations from the simple A-type fabric (Figure 15).

[38] The conditions under which B-type fabric is expected to dominate (i.e., high stress, moderate-to-high water content) are restricted to the extreme wedge corner where isolation of the region may occur because of a reduction in viscous coupling of the convecting mantle with the downgoing plate [*Kneller et al.*, 2005, 2007]. Although *Kneller et al.* [2007] demonstrate that the exact across-arc location of this transition will depend on several parameters (e.g., slab dip, slab age, slab hydration, wedge rheology), B-type fabric is not expected to exist in the higher-temperature (lower-stress) mantle wedge beneath the arc and back arc (Figures 15a and 15b, right sides of each diagram). If B-type fabric does exist, then a transition in LPO should occur within the fore-arc wedge along with a corresponding transition in observed fast direction orientations at the surface. For 2-D corner flow, such a transition would predict arc-parallel fast directions in the fore arc changing to plate motion parallel in the arc and back arc, a pattern that is clearly observed in Honshu and Ryukyu [*Nakajima and Hasegawa*, 2004; *Long and van der Hilst*, 2005; *Nakajima et al.*, 2006].

[39] The presence of melt in deforming olivine samples has also been shown to influence the orientation of fabric relative to shear. When additional "pinning" phases (e.g., chromite or FeS) are present in peridotite, a reduction in permeability occurs and results in the segregation of melt into bands separated by relatively melt-free crystal lenses [*Holtzman et al.*, 2003]. As the material (solid+melt) deforms, strain is partitioned into the melt bands, causing compaction of the crystal lenses and subsequent strain oriented approximately perpendicular to the large-scale shear direction. Thus, the primary implication of oriented melt bands, if the *a* axes of olivine in the crystal lenses align subparallel to shear, is that the fast seismic direction under these conditions will be perpendicular to overall flow. It is unclear, however, how long these effects on LPO will remain because the melt bands tend to migrate through a region, leaving the crystal lenses behind to have their LPO reset to that imparted by the dominant flow field. Nonetheless, even if melt bands are transient features in the

wedge, anisotropy produced by the bands themselves (i.e., SPO) could be significant, and could also produce a fast seismic polarization normal to overall flow, if the melt bands are oriented subvertically. The most likely location for the high melt fractions required for melt band formation, and thus deviations in *a* axis orientations from flow-parallel, is beneath the volcanic arc (i.e., arc-parallel fast directions close to the arc and arc-normal fast directions in the fore arc and back arc; see *Abt and Fischer* [2008, Figure 13] for predicted splitting parameters from such a fabric geometry).

5.2. Proposed Arc-Parallel Mantle Wedge Flow Beneath Costa Rica and Nicaragua

[40] The observed pattern of shear wave splitting fast directions and tomographically imaged anisotropic structure strongly suggest that an arc-parallel fast fabric exists over broad regions of the Central American mantle wedge. The most straightforward explanation for this fabric is that it represents olivine *a* axes aligned with roughly arc-parallel flow. Both arc-parallel fast directions (Figures 3 and 6) and model *a* axes (Figures 10 and 11) extend into the back arc, making 2-D corner flow an unlikely scenario, even with B-type fabric. In addition, the subset of splitting measurements in the northwest Nicaraguan fore arc display fast directions which rotate from arc-normal closer to the trench to arc-parallel beneath the arc (Figure 6a), opposite of the observed trend in Japan [*Long and van der Hilst*, 2005; *Nakajima et al.*, 2006]. This pattern would be expected for along-arc flow and B-type fabric in the extreme wedge corner (Figure 15b). However, while this pattern in the data is reflected in the inversion (Figure 10a), it is not robustly retrieved (Figure 10b), largely because this region lies at the edge of the model. Nor is this pattern as clearly observed in other along-arc segments. Along-arc flow is schematically depicted relative to the anisotropic model in Figure 10b. *Mehl et al.* [2003] observed a horizontal foliation plane concurrent with arc-parallel *a* axes in the accreted Talkeetna arc in Alaska, but our current data in Central America cannot distinguish between a horizontal and vertical shear plane; therefore, we illustrate both possibilities (Figure 10b).

[41] Could 2-D corner flow still be possible in the mantle wedge if melt effects are considered, such as viscosity variations associated with concentrated melt bands that reorient olivine LPO so that *a* axes are arc-parallel [e.g., *Holtzman et al.*, 2003] (Figure 15a, left side), and/or the SPO anisotropy of the melt pockets/bands themselves [*Zimmerman et al.*, 1999; *Holtzman et al.*, 2003]? Although this type of model cannot be ruled out on seismological grounds alone, it seems unlikely that sufficiently large melt fractions exist throughout the entire mantle wedge. In particular, high Vp/Vs ratios, thought to represent melt rising to the arc from near the top of the slab in Nicaragua [*Syracuse et al.*, 2008] are confined to a tabular volume beneath the arc, and do not extend into the back-arc wedge where arc-parallel fast anisotropy is also observed (Figures 10 and 11). This interpretation is also consistent with the concentration of present-day magmatism at a volcanic front that is narrow in the arc-normal direction, although small amounts of magmatism do occur further into the back arc [e.g., *Walker et al.*, 1995].

[42] The implications of the three pockets of arc-normal *a* axes at mantle wedge depths in our model (Figures 10 and 11) are not entirely clear. These features are reflected in the shear wave splitting measurements (Figures 3 and 6), but only one of these zones is retrieved with total angular misfits of less than 35° in the recovery tests (Figure 10b), and its location at the very northern edge of the model still makes it somewhat suspect. If these arc-normal zones are real, they may represent a small-scale variation in the flow pattern. For example, upwellings (e.g., buoyant diapirs [*Hall and Kincaid*, 2001; *Behn et al.*, 2007] or downwellings (e.g., foundering arc lithosphere [*Behn et al.*, 2007]) could perturb an otherwise predominantly arc-parallel flow field, as could variable degrees of mantle entrainment with the subducting plate. Another possibility is that these arc-normal volumes represent a localized zone with particularly high melt content. However, none of them are spatially correlated with the volumes of highest Vp/Vs imaged by *Syracuse et al.* [2008].

5.3. Geochemical Evidence for Arc-Parallel Flow

[43] Geochemical data provide key evidence that along-arc mantle wedge flow is the correct interpretation for the observed arc-parallel fast anisotropy. Northwest arc-parallel flow has been invoked to explain a variety of along-arc geochemical variations [*Herrstrom et al.*, 1995; *Abratis and Wörner*, 2001; *Hoernle et al.*, 2008], although, as described in the introduction, alternative models have also been proposed [*Feigenson et al.*, 2004; *Goss and Kay*, 2006].

[44] *Hoernle et al.* [2008] trace the source of high $^{208}Pb/^{204}Pb$ ratios and low $^{143}Nd/^{144}Nd$ ratios in recent (<6 My) arc volcanics in central Costa Rica to the Galapagos Seamounts that lie on the subducting Cocos Plate (Figure 1). The $^{208}Pb/^{204}Pb$ ratios decline and the $^{143}Nd/^{144}Nd$ ratios increase from central Costa Rica to the northwest, until they reach MORB-like values in northwest Nicaragua that match the composition of the locally subducting Cocos Plate crust. These results indicate northwest flow of mantle bearing the seamount signature and its progressive dilution as it mixes with more typical mantle wedge peridotite. Constraints on the time at which the seamount signature was first introduced into the wedge suggest mantle wedge flow at a minimum velocity of 63–190 mm/a, comparable to the subduction rate of the Cocos Plate (~85 mm/a [*DeMets*, 2001]) [*Hoernle et al.*, 2008]. This model could also help to explain other geochemical trends observed along the arc, for example the northwestward increase in Ba/La, U/Th, and Ba/Th and decrease in La/Yb [e.g., *Herrstrom et al.*, 1995; *Patino et al.*, 2000; *Carr et al.*, 2003], if the Galapagos seamount component had melt-like properties when it entered the wedge [*Hoernle et al.*, 2008]. However, these ratios could also reflect variations in sediment signatures entering the wedge locally with slab fluids (Ba/La, U/Th, and Ba/Th) or the local degree of melting (La/Yb), as has been previously proposed [*Herrstrom et al.*, 1995; *Patino et al.*, 2000; *Carr et al.*, 2003].

5.4. Drivers for Arc-Parallel Flow and Implications for Mantle Depletion

[45] Flow along the strike of the subducting Cocos Plate could be driven by interactions with the slab edge, slab rollback, and oblique subduction (Figure 10b). However, it is also possible that global mantle convection currents [e.g., *Conrad and Lithgow-Bertelloni*, 2004] contribute to flow that does not conform to the predictions of 2-D corner flow driven by local plate motion. Each of these sources of along-arc flow may not individually be strong enough to overcome the expected plate motion-parallel flow generated by entrainment with the subducting slab, but in concert they may constitute the necessary driving force, particularly if they are aided by weak slab-mantle coupling or other rheological factors.

[46] Tectonic variations within the Nicaragua–Costa Rica subduction zone (section 2) provide a basis for inferring possible local drivers for along-arc flow. Viscous flow modeling has shown that along-arc flow may be possible if slab rollback occurs in the vicinity of a slab edge [*Kincaid and Griffiths*, 2003; *Funiciello et al.*, 2006], and this scenario has been proposed in other subduction zones (e.g., Kamchatka [*Peyton et al.*, 2001] and Tonga [*Smith et al.*, 2001]). The decrease in deep subduction-related seismicity [*Protti et al.*, 1994; *Syracuse et al.*, 2008] and the termination of active arc volcanism in southeast Costa Rica [*Carr et al.*, 2003] indicate the existence of the southeast edge of the Cocos Plate. Because trench motion rates depend on global plate motion reference frame, it is difficult to infer whether the trench in Nicaragua and Costa Rica is in retreat or advance in an absolute sense [*Lallemand et al.*, 2008; *Schellart et al.*, 2008]. However, for models in which significant along-arc variations in trench migration rate exist [*Schellart et al.*, 2008], the trench in northern Nicaragua is 1–2 cm/a in retreat relative to the trench in Costa Rica. This latter tendency in present-day trench motion correlates with the geologic record. The modern arc in northern Nicaragua is offset by more than 125 km trenchward relative to arc position in the early Miocene, a much greater shift than is found in Costa Rica [*Weinberg*, 1992; *Plank et al.*, 2002; *Alvarado et al.*, 2007]. Greater slab and trench rollback in Nicaragua could draw wedge material to the northwest. In addition, whereas present-day extension occurs at an average rate of 5 mm/a in northwest Nicaragua, arc-normal deformation shifts along the arc to compression in southeast Nicaragua [*Turner et al.*, 2007]. A slight obliquity of subduction [*DeMets*, 2001] may influence entrained flow within the wedge, perhaps by generating a toroidal component of motion [*Kneller and van Keken*, 2008], and northwest transport of the fore-arc sliver of the upper plate [*Turner et al.*, 2007] could also affect wedge flow.

[47] Large changes in slab dip, for example as observed in the Nazca plate subducting beneath South America, can induce significant along-arc flow [*Kneller and van Keken*, 2007 and 2008]. However, this mechanism does not appear to be a dominant factor beneath Nicaragua and Costa Rica. First, changes in slab dip inferred from earthquake hypocenters and velocity tomography [*Syracuse et al.*, 2008] are less than about 15–20°, and initial numerical modeling incorporating this slab shape does not show significant deviations from 2-D corner flow (P. E. van Keken, personal communication, 2008). Second, the modest decrease in slab dip occurs to the southeast, which would predict southeastern along-arc flow, if any along-arc flow were produced. This prediction would contradict

the northwest flow indicated by geochemical data [*Herrstrom et al.*, 1995; *Abratis and Wörner*, 2001; *Hoernle et al.*, 2008].

[48] If along-arc flow is generated by interactions between slab shape and position, plate motions, and larger mantle flow patterns, the rheology of the mantle wedge and slab-wedge interface could help to sustain it with distance along the arc and in time. Decoupling of the mantle wedge from the subducting Cocos Plate may be caused by a low-viscosity layer along the slab interface, perhaps as a result of hydrous phases. Seismic evidence for low-velocity layers in the subducting oceanic crust [*Abers et al.*, 2003; *Abers*, 2005] and mantle [*Syracuse et al.*, 2008] suggest that water may be carried to depths of 150 km or more. When released, these fluids may cause serpentinization or the creation of chlorite in the overlying mantle, as is observed in the fore arc [*DeShon and Schwartz*, 2004], but also perhaps at greater depths. Although many subduction zone thermal models predict serpentine to be stable only in the shallow mantle wedge corner above the subducting plate [e.g., *Bostock et al.*, 2002; *Hyndman and Peacock*, 2003; *Abers et al.*, 2006; *Arcay et al.*, 2007; *Cagnioncle et al.*, 2007], and not above the slab interface at greater depths where we observe arc-parallel *a* axes (down to 150 km, Figure 10), the chlorite stability field may persist more deeply in a thin layer just above the slab [*Cagnioncle et al.*, 2007], thereby providing a possible means of decoupling the slab from most of the mantle wedge. In addition, these thermal models assume 2-D corner flow, and one of their basic characteristics is the upwelling of relatively hot back-arc wedge material into the wedge corner before it is dragged down with the plate. With along-arc flow near the slab, mantle wedge temperatures above the slab surface may be significantly lower, thereby allowing both serpentine and chlorite to exist and decouple the slab from the wedge at greater depths. Broader low-viscosity zones likely also exist further into the mantle wedge, produced by the hydrated wedge peridotite and partial melt seen in velocity and attenuation tomography [*Syracuse et al.*, 2008; *Rychert et al.*, 2008]. This type of low-viscosity channel could help to focus along-arc flow, thus enhancing the alignment of olivine *a* axes parallel to the arc [*Conder and Wiens*, 2007].

[49] Along-arc flow in the mantle wedge would have a variety of implications for subduction zone melting models. It would alter slab and wedge temperature structure, as has already been demonstrated in a limited number of 3-D flow scenarios [e.g., *Kincaid and Griffiths*, 2004]. In addition, it could affect the degree of depletion of the mantle wedge material flowing into the fluid-fluxed region of potential melting beneath a given segment of the arc. In 2-D corner flow models, upwelling material from the back-arc wedge is likely to be less depleted and would therefore be more easily melted [e.g., *Cagnioncle et al.*, 2007]. However, if along-arc flow occurs in the mantle wedge where arc magmas originate, then a progressive depletion in the mantle source would be expected. Progressive depletion from Costa Rica to Nicaragua is consistent with geochemical trends [*Herrstrom et al.*, 1995], although it is not required given the possibility of along-arc variations in the degree of new melting or local input from the slab.

6. Conclusions

[50] Tomographic inversion of shear wave splitting observations reveals anisotropic structure that is not consistent with 2-D corner flow in the Central American mantle wedge. Well-resolved arc-parallel olivine *a* axes are found in the mantle beneath the arc and back arc, well outside the shallow (cold) wedge corner where B-type olivine fabrics may exist and align olivine *a* axes normal to flow. The arc-parallel fast fabric also occupies too broad a volume to be easily explained by the effects of partial melt. We therefore conclude that the wedge anisotropy is best explained by olivine *a* axes aligned parallel to along-arc flow. This interpretation is corroborated by $^{208}Pb/^{204}Pb$ and $^{143}Nd/^{144}Nd$ trends that indicate northwest transport of material bearing the signature of the Galapagos seamounts at a minimum velocity of 63–190 mm/a [*Hoernle et al.*, 2008]. Flow along the strike of the slab in the mantle wedge may be driven by the combined effects of slab rollback, the slab edge in Costa Rica, and along-strike components of plate motion, although broader patterns of mantle convection could also play a role.

Acknowledgments

[51] We thank Ellen Syracuse for the event hypocenters, Kaj Hoernle for the isotope analyses and interpretations, and Don Forsyth and Terry Plank for many useful conversations. Martha Savage and an anonymous reviewer provided constructive reviews. Thanks also to Pedro Pérez, Allan Morales, Catherine Rychert, Ellen Syracuse, Laura MacKenzie, Mariela Salas-de la Cruz, Alexis Walker, Gustavo Reyes, and Tim Parker for their hard work with the acquisition of the seismic data. The IRIS/PASSCAL program provided seismometers for

the TUCAN Seismic Experiment. This research and the TUCAN Seismic Experiment were supported by the NSF-MARGINS program through awards OCE-0203607, OCE-0203650, and EAR-0742282.

References

Abers, G. A. (2005), Seismic low-velocity layer at the top of subducting slabs: Observations, predictions, and systematics, *Phys. Earth Planet. Inter.*, *149*, 7–29, doi:10.1016/j.pepi.2004.10.002.

Abers, G. A., T. Plank, and B. R. Hacker (2003), The wet Nicaraguan slab, *Geophys. Res. Lett.*, *30*(2), 1098, doi:10.1029/2002GL015649.

Abers, G. A., P. E. van Keken, E. A. Kneller, A. Ferris, and J. C. Stachnik (2006), The thermal structure of subduction zones constrained by seismic imaging: Implications for slab dehydration and wedge flow, *Earth Planet. Sci. Lett.*, *241*, 387–397, doi:10.1016/j.epsl.2005.11.055.

Abramson, E. H., J. M. Brown, L. J. Slutsky, and J. Zaug (1997), The elastic constants of San Carlos olivine to 17 GPa, *J. Geophys. Res.*, *102*, 12,253–12,263, doi:10.1029/97JB00682.

Abratis, M., and G. Wörner (2001), Ridge collision, slab-window formation, and the flux of Pacific asthenosphere in the Caribbean realm, *Geology*, *29*, 127–130, doi:10.1130/0091-7613(2001)029<0127:RCSWFA>2.0.CO;2.

Abt, D. L., and K. M. Fischer (2008), Resolving three-dimensional anisotropic structure with shear-wave splitting tomography, *Geophys. J. Int.*, *173*, 859–886, doi:10.1111/j.1365-246X.2008.03757.x.

Alvarado, G. E., et al. (2007), *Central America: Geology, Resources, and Hazards*, edited by J. Bundschuh and G. Alvarado, pp. 345–394, Taylor and Francis, Leiden, Netherlands.

Anderson, M. L., G. Zandt, E. Triep, M. Fouch, and S. Beck (2004), Anisotropy and mantle flow in the Chile-Argentina subduction zone from shear wave splitting analysis, *Geophys. Res. Lett.*, *31*, L23608, doi:10.1029/2004GL020906.

Anderson, O. L., and D. G. Isaak (1995), Elastic constants of mantle minerals at high temperature, in *Mineral Physics and Crystallography: A Handbook of Physical Constants*, edited by T. J. Ahrens, pp. 64–97, AGU, Washington, D. C.

Anglin, D. K., and M. J. Fouch (2005), Seismic anisotropy in the Izu-Bonin subduction system, *Geophys. Res. Lett.*, *32*, L09307, doi:10.1029/2005GL022714.

Arcay, D., E. Tric, and M.-P. Doin (2007), Slab surface temperature in subduction zones: Influence of interpolate decoupling depth and upper plate thinning processes, *Earth Planet. Sci. Lett.*, *255*, 324–338, doi:10.1016/j.epsl.2006.12.027.

Audoine, E., M. K. Savage, and K. Gledhill (2004), Anisotropic structure under a back arc spreading region, the Taupo Volcanic Zone, New Zealand, *J. Geophys. Res.*, *109*, B11305, doi:10.1029/2003JB002932.

Babuska, V., and M. Cara (1991), *Seismic Anisotropy in the Earth*, 217 pp., Kluwer, Dordrecht, Netherlands.

Barckhausen, U., C. R. Ranero, R. von Huene, S. C. Cande, and H. A. Roeser (2001), Revised tectonic boundaries in the Cocos Plate off Costa Rica: Implications for the segmentation of the convergent margin and for plate tectonic models, *J. Geophys. Res.*, *106*, 19,207–19,220, doi:10.1029/2001JB000238.

Behn, M. D., G. Hirth, and P. B. Kelemen (2007), Trench-parallel anisotropy produced by foundering of arc lower crust, *Science*, *317*, 108–111, doi:10.1126/science.1141269.

Blackman, D. K., and J.-M. Kendall (2002), Seismic anisotropy in the upper mantle: 2. Predictions for current plate boundary flow models, *Geochem. Geophys. Geosyst.*, *3*(9), 8602, doi:10.1029/2001GC000247.

Bostock, M. G., R. D. Hyndman, S. Rondenay, and S. M. Peacock (2002), An inverted continental Moho and serpentinization of the forearc mantle, *Nature*, *417*, 536–538, doi:10.1038/417536a.

Buttles, J., and P. Olsen (1998), A laboratory model of subduction zone anisotropy, *Earth Planet. Sci. Lett.*, *164*, 245–262, doi:10.1016/S0012-821X(98)00211-8.

Bystricky, M., K. Kunze, L. Burlini, and J.-P. Burg (2000), High shear strain of olivine aggregates: Rheological and seismic consequences, *Science*, *290*, 1564–1567, doi:10.1126/science.290.5496.1564.

Cagnioncle, A. M., E. M. Parmentier, and L. T. Elkins-Tanton (2007), Effect of solid flow above a subducting slab on water distribution and melting at convergent plate boundaries, *J. Geophys. Res.*, *112*, B09402, doi:10.1029/2007JB004934.

Carr, M. J., M. D. Feigenson, L. C. Patino, and J. A. Walker (2003), Volcanism and geochemistry in Central America: Progress and problems, in *Inside the Subduction Factory*, *Geophysical Monogr. Ser.*, vol. 138, edited by J. Eiler, pp. 153–174, AGU, Washington, D. C.

Christensen, D. H., G. A. Abers, and T. L. McKnight (2003), Mantle anisotropy beneath the Alaska Range inferred from S-wave splitting observations: Results from BEAAR, *Eos Trans. AGU*, *84*(46), Fall Meet. Suppl., Abstract S31C-0782.

Conder, J. A., and D. A. Wiens (2007), Rapid mantle flow beneath the Tonga volcanic arc, *Earth Planet. Sci. Lett.*, *264*, 299–307, doi:10.1016/j.epsl.2007.10.014.

Conrad, C. P., and C. Lithgow-Bertelloni (2004), The temporal evolution of plate driving forces: Importance of "slab suction" versus "slab pull" during the Cenozoic, *J. Geophys. Res.*, *109*, B10407, doi:10.1029/2004JB002991.

DeMets, C. (2001), A new estimate for present-day Cocos-Caribbean plate motion: Implications for slip along the Central American volcanic arc, *Geophys. Res. Lett.*, *28*, 4043–4046, doi:10.1029/2001GL013518.

DeShon, H. R., and S. Y. Schwartz (2004), Evidence for serpentinization of the forearc mantle wedge along the Nicoya Peninsula, Costa Rica, *Geophys. Res. Lett.*, *31*, L21611, doi:10.1029/2004GL021179.

Elming, S. A., and T. Rasmussen (1997), Results of magnetotelluric and gravimetric measurements in western Nicaragua, Central America, *Geophys. J. Int.*, *128*, 647–658, doi:10.1111/j.1365-246X.1997.tb05326.x.

Faccenda, M., L. Burlini, T. V. Gerya, and D. Mainprice (2008), Fault-induced seismic anisotropy by hydration in subducting oceanic plates, *Nature*, *455*, 1097–1101, doi:10.1038/nature07376.

Feigenson, M. D., M. J. Carr, S. V. Maharaj, S. Juliano, and L. L. Bolge (2004), Lead isotope composition of Central American volcanoes: Influence of the Galapagos plume, *Geochem. Geophys. Geosyst.*, *5*, Q06001, doi:10.1029/2003GC000621.

Fischer, K. M., E. M. Parmentier, A. R. Stein, and E. R. Wolf (2000), Modeling anisotropy and plate-driven flow in the Tonga subduction zone back arc, *J. Geophys. Res.*, *105*, 16,181–16,191, doi:10.1029/1999JB900441.

Frisillo, A. L., and G. R. Barsch (1972), Measurement of single-crystal elastic constants of bronzite as a function of pressure and temperature, *J. Geophys. Res.*, *77*, 6360–6384, doi:10.1029/JB077i032p06360.

Funiciello, F., M. Moroni, C. Pimomallo, C. Faccenna, A. Cenedese, and H. A. Bui (2006), Mapping mantle flow during retreating subduction: Laboratory models analyzed by feature tracking, *J. Geophys. Res.*, *111*, B03402, doi:10.1029/2005JB003792.

Goss, A. R., and S. M. Kay (2006), Steep REE patterns and enriched Pb isotopes in southern Central American arc magmas: Evidence for forearc subduction erosion?, *Geochem. Geophys. Geosyst.*, *7*, Q05016, doi:10.1029/2005GC001163.

Hall, C. E., K. M. Fischer, E. M. Parmentier, and D. K. Blackman (2000), The influence of plate motions on three-dimensional back-arc mantle flow and shear-wave splitting, *J. Geophys. Res.*, *105*, 28,009–28,033, doi:10.1029/2000JB900297.

Hall, P. S., and C. Kincaid (2001), Diapiric flow at subduction zones: A recipe for rapid transport, *Science*, *292*, 2472–2475, doi:10.1126/science.1060488.

Herrstrom, E. A., M. K. Reagan, and J. D. Morris (1995), Variations in lava composition associated with flow of asthenosphere beneath southern Central America, *Geology*, *23*, 617–620, doi:10.1130/0091-7613(1995)023<0617:VILCAW>2.3.CO;2.

Hoernle, K. (2008), Arc-parallel flow in the mantle wedge beneath Costa Rica and Nicaragua, *Nature*, *451*, 1094–1098, doi:10.1038/nature06550.

Holtzman, B. K., D. L. Kohlstedt, M. E. Zimmerman, F. Heidelbach, T. Hiraga, and J. Hustoft (2003), Melt segregation and strain partitioning: Implications for seismic anisotropy and mantle flow, *Science*, *301*, 1227–1230, doi:10.1126/science.1087132.

Huang, B.-S., W.-G. Huang, W.-T. Liang, R.-J. Rau, and N. Hirata (2006), Anisotropy beneath an active collision orogen of Taiwan: Results from across islands array observations, *Geophys. Res. Lett.*, *33*, L24302, doi:10.1029/2006GL027844.

Hung, S.-H., and D. W. Forsyth (1998), Modeling anisotropic wave propagation in oceanic inhomogeneous structures using the parallel multi-domain pseudo spectral method, *J. Geophys. Res.*, *133*, 726–740.

Husen, S., R. Quintero, E. Kissling, and B. Hacker (2003), Subduction-zone structure and magmatic processes beneath Costa Rica constrained by local earthquake tomography and petrological modeling, *Geophys. J. Int.*, *155*, 11–32, doi:10.1046/j.1365-246X.2003.01984.x.

Hyndman, R. D., and S. M. Peacock (2003), Serpentinization of the forearc mantle, *Earth Planet. Sci. Lett.*, *212*, 417–432, doi:10.1016/S0012-821X(03)00263-2.

Iinuma, T., M. Protti, K. Obana, V. Gonzalez, R. Van der Laat, T. Kato, S. Miyazaki, Y. Kaneda, and E. Hernandez (2004), Inter-plate coupling in the Nicoya Peninsula, Costa Rica, as deduced from a trans-peninsula GPS experiment, *Earth and Planet. Sci. Lett.*, *223*, 203–212.

Ismaïl, W. B., and D. Mainprice (1998), An olivine fabric database: An overview of upper mantle fabrics and anisotropy, *Tectonophysics*, *296*, 145–157, doi:10.1016/S0040-1951(98)00141-3.

Jung, H., and S. Karato (2001), Water-induced fabric transitions in olivine, *Science*, *293*, 1460–1463, doi:10.1126/science.1062235.

Jung, H., I. Katayama, Z. Jiang, T. Hiraga, and S. Karato (2006), Effect of water and stress on the lattice-preferred orientation of olivine, *Tectonophysics*, *421*, 1–22, doi:10.1016/j.tecto.2006.02.011.

Katayama, I., and S. Karato (2006), Effect of temperature on the B- to C-type olivine fabric transition and implication for flow pattern in subduction zones, *Phys. Earth Planet. Inter.*, *157*, 33–45, doi:10.1016/j.pepi.2006.03.005.

Kincaid, C., and R. W. Griffiths (2003), Laboratory models of the thermal evolution of the mantle during rollback subduction, *Nature*, *425*, 58–62, doi:10.1038/nature01923.

Kincaid, C., and R. W. Griffiths (2004), Variability in flow and temperatures within mantle subduction zones, *Geochem. Geophys. Geosyst.*, *5*, Q06002, doi:10.1029/2003GC000666.

Kincaid, C., and P. S. Hall (2003), Role of back arc spreading in circulation and melting at subduction zones, *J. Geophys. Res.*, *108*(B5), 2240, doi:10.1029/2001JB001174.

Kneller, E. A., and P. E. van Keken (2007), Trench-parallel flow and seismic anisotropy in the Mariana and Andean subduction systems*Nature*, *450*, 1222–1225, doi:10.1038/nature06429.

Kneller, E. A., and P. E. van Keken (2008), Effect of three-dimensional slab geometry on deformation in the mantle wedge: Implications for shear wave anisotropy, *Geochem. Geophys. Geosyst.*, *9*, Q01003, doi:10.1029/2007GC001677.

Kneller, E. A., P. E. van Keken, S. Karato, and J. Park (2005), B-type olivine fabric in the mantle wedge: Insights from high-resolution non-Newtonian subduction zone models, *Earth Planet. Sci. Lett.*, *237*, 781–797, doi:10.1016/j.epsl.2005.06.049.

Kneller, E. A., P. E. van Keken, I. Katayama, and S. Karato (2007), Stress, strain, and B-type olivine fabric in the fore-arc mantle: Sensitivity tests using high-resolution steady-state subduction zone models, *J. Geophys. Res.*, *112*, B04406, doi:10.1029/2006JB004544.

Lallemand, S., A. Heuret, C. Faccenna, and F. Funiciello (2008), Subduction dynamics as revealed by trench migration, *Tectonics*, *27*, TC3014, doi:10.1029/2007TC002212.

Lassak, T. M., M. J. Fouch, C. E. Hall, and E. Kaminiski (2006), Seismic characterization of mantle flow in subduction systems: Can we resolve a hydrated mantle wedge?, *Earth Planet. Sci. Lett.*, *243*, 632–649, doi:10.1016/j.epsl.2006.01.022.

Levin, V., D. Droznin, J. Park, and E. Gordeev (2004), Detailed mapping of seismic anisotropy with local shear waves in southeastern Kamchatka, *Geophys. J. Int.*, *158*, 1009–1023, doi:10.1111/j.1365-246X.2004.02352.x.

Long, M. D., and P. G. Silver (2008), The subduction zone flow field from seismic anisotropy: A global view, *Science*, *319*, 315–318, doi:10.1126/science.1150809.

Long, M. D., and R. D. van der Hilst (2005), Upper mantle anisotropy beneath Japan from shear wave splitting, *Phys. Earth Planet. Inter.*, *151*, 206–222, doi:10.1016/j.pepi.2005.03.003.

Long, M. D., and R. D. van der Hilst (2006), Shear wave splitting from local events beneath the Ryukyu arc: Trench parallel anisotropy in the mantle wedge, *Phys. Earth Planet. Inter.*, *155*, 300–312, doi:10.1016/j.pepi.2006.01.003.

Lowman, J. P., L. T. Pinero-Feliciangeli, J.-M. Kendall, and M. H. Shahnas (2007), Influence of convergent plate boundaries on upper mantle flow and implications for seismic anisotropy, *Geochem. Geophys. Geosyst.*, *8*, Q08007, doi:10.1029/2007GC001627.

Lundgren, P., M. J. Protti, A. Donnellan, M. Heflin, E. Hernandez, and D. Jefferson (1999), Seismic cycle and plate margin deformation in Costa Rica: GPS observations from 1994 to 1997, *J. Geophys. Res.*, *104*, 28,915–28,926, doi:10.1029/1999JB900283.

MacKenzie, L., G. A. Abers, K. M. Fischer, E. M. Syracuse, J. M. Protti, V. Gonzalez, and W. Strauch (2008), Crustal structure along the southern Central American volcanic front, *Geochem. Geophys. Geosyst.*, *9*, Q08S09, doi:10.1029/2008GC001991.

Mainprice, D., and P. G. Silver (1993), Interpretation of SKS-waves using samples from the subcontinental lithosphere, *Phys. Earth Planet. Inter.*, *78*, 257–280, doi:10.1016/0031-9201(93)90160-B.

Mainprice, D., A. Tommasi, H. Couvy, P. Cordier, and D. J. Frost (2005), Pressure sensitivity of olivine slip systems and seismic anisotropy of Earth's upper mantle, *Nature*, *433*, 731–733, doi:10.1038/nature03266.

Matcham, I., M. K. Savage, and K. R. Kendall (2000), Distribution of seismic anisotropy in the subduction zone beneath the Wellington region, New Zealand, *Geophys. J. Int.*, *140*, 1–10, doi:10.1046/j.1365-246x.2000.00928.x.

McKenzie, D. (1979), Finite deformation during fluid flow, *Geophys. J. R. Astron. Soc.*, *58*, 689–715.

Mehl, L., B. R. Hacker, G. Hirth, and P. B. Kelemen (2003), Arc-parallel flow within the mantle wedge: Evidence from the accreted Talkeetna arc, south central Alaska, *J. Geophys. Res.*, *108*(B8), 2375, doi:10.1029/2002JB002233.

Michibayshi, K., N. Abe, A. Okamoto, T. Satsukawa, and K. Michikura (2006), Seismic anisotropy in the uppermost mantle, back-arc region of the northeast Japan arc: Petrophysical analyses of Ichinomegata peridotite xenoliths, *Geophys. Res. Lett.*, *33*, L10312, doi:10.1029/2006GL025812.

Mizukami, T., S. R. Wallis, and J. Yamamoto (2004), Natural examples of olivine lattice preferred orientation patterns with a flow-normal a-axis maximum, *Nature*, *427*, 432–436, doi:10.1038/nature02179.

Montagner, J.-P., and D. L. Anderson (1989), Petrological constraints on seismic anisotropy, *Phys. Earth Planet. Inter.*, *54*, 82–105, doi:10.1016/0031-9201(89)90189-1.

Morley, A. M., G. W. Stuart, J.-M. Kendall, and M. Reyners (2006), Mantle wedge anisotropy in the Hikurangi subduction zone, central North Island, New Zealand, *Geophys. Res. Lett.*, *33*, L05301, doi:10.1029/2005GL024569.

Nakajima, J., and A. Hasegawa (2004), Shear-wave polarization and subduction-induced flow in the mantle wedge of northeastern Japan, *Earth Planet. Sci. Lett.*, *225*, 365–377, doi:10.1016/j.epsl.2004.06.011.

Nakajima, J., J. Shimizu, S. Hori, and A. Hasegawa (2006), Shear-wave splitting beneath the southwestern Kurile arc and northeastern Japan arc: A new insight into mantle return flow, *Geophys. Res. Lett.*, *33*, L05305, doi:10.1029/2005GL025053.

Norabuena, E., et al. (2004), Geodetic and seismic constraints on some seismogenic zone processes in Costa Rica, *J. Geophys. Res.*, *109*, B11403, doi:10.1029/2003JB002931.

Patino, L. C., M. J. Carr, and M. D. Feigenson (2000), Local and regional variations in Central American arc lavas controlled by variations in subducted sediment input, *Contrib. Mineral. Petrol.*, *138*, 265–283, doi:10.1007/s004100050562.

Peyton, V., V. Levin, J. Park, M. Brandon, J. Lees, E. Gordeev, and A. Ozerov (2001), Mantle flow at a slab edge: Seismic anisotropy in the Kamchatka region, *Geophys. Res. Lett.*, *28*, 379–382, doi:10.1029/2000GL012200.

Plank, T., V. Balzer, and M. Carr (2002), Nicaraguan volcanoes record paleooceanographic changes accompanying closure of the Panama gateway, *Geology*, *30*, 1087–1090, doi:10.1130/0091-7613(2002)030<1087:NVRPCA>2.0.CO;2.

Polet, J., P. G. Silver, S. Beck, T. Wallace, G. Zandt, S. Ruppert, R. Kind, and A. Rudloff (2000), Shear wave anisotropy beneath the Andes from the BANJO, SEDA, and PISCO experiments, *J. Geophys. Res.*, *105*, 6287–6304, doi:10.1029/1999JB900326.

Pozgay, S. H., D. A. Wiens, J. A. Conder, H. Shiobara, and H. Sugioka (2007), Complex mantle flow in the Mariana subduction system: Evidence from shear wave splitting, *Geophys. J. Int.*, *170*, 371–386, doi:10.1111/j.1365-246X.2007.03433.x.

Protti, M., F. Gundel, and K. McNally (1994), The geometry of the Wadditi-Benioff zone under southern Central America and its tectonic significance: Results from a high resolution local seismographic network, *Phys. Earth Planet. Inter.*, *84*, 271–287, doi:10.1016/0031-9201(94)90046-9.

Ribe, N. M. (1989), Seismic anisotropy and mantle flow, *J. Geophys. Res.*, *94*, 4213–4223, doi:10.1029/JB094iB04p04213.

Rümpker, G., and P. G. Silver (1998), Apparent shear-wave splitting parameters in the presence of vertically varying anisotropy, *Geophys. J. Int.*, *135*, 790–800, doi:10.1046/j.1365-246X.1998.00660.x.

Russo, R. M., and P. G. Silver (1994), Trench-parallel flow beneath the Nazca Plate from seismic anisotropy, *Science*, *263*, 1105–1111, doi:10.1126/science.263.5150.1105.

Rychert, C. A., K. M. Fischer, G. A. Abers, T. Plank, E. Syracuse, J. M. Protti, V. Gonzalez, and W. Strauch (2008), Strong along-arc variations in attenuation in the mantle wedge beneath Costa Rica and Nicaragua, *Geochem. Geophys. Geosyst.*, *9*, Q10S10, doi:10.1029/2008GC002040.

Schellart, W. P., D. R. Stegman, and J. Freeman (2008), Global trench migration velocities and slab migration induced upper mantle volume fluxes: Constraints to an Earth reference frame based on minimizing viscous dissipation, *Earth Sci. Rev.*, *88*, 118–144, doi:10.1016/j.earscirev.2008.01.005.

Silver, P. G., and W. W. Chan (1991), Shear wave splitting and subcontinental mantle deformation, *J. Geophys. Res.*, *96*, 16,429–16,454, doi:10.1029/91JB00899.

Silver, P. G., and M. K. Savage (1994), The interpretation of shear-wave splitting parameters in the presence of two anisotropic layers, *Geophys. J. Int.*, *119*, 949–963, doi:10.1111/j.1365-246X.1994.tb04027.x.

Smith, G. P., D. A. Wiens, K. M. Fischer, L. M. Dorman, S. C. Webb, and J. H. Hildebrand (2001), A complex pattern of flow win the Lau backarc, *Science*, *292*, 713–716, doi:10.1126/science.1058763.

Syracuse, E. M., and G. A. Abers (2006), Global compilation of variations in slab depth beneath arc volcanoes and implications, *Geochem. Geophys. Geosyst.*, *7*, Q05017, doi:10.1029/2005GC001045.

Syracuse, E. M., G. A. Abers, K. M. Fischer, L. MacKenzie, C. Rychert, J. M. Protti, V. Gonzalez, and W. Strauch (2008), Seismic tomography and earthquake locations in the Nicaraguan and Costa Rican upper mantle, *Geochem. Geophys. Geosyst.*, *9*, Q07S08, doi:10.1029/2008GC001963.

Tarantola, A. (1987), *Inverse Problem Theory: Methods for Data Fitting and Model Parameter Estimation*, 613 pp., Elsevier, Amsterdam.

Turner, H. L., P. LaFemina, A. Saballos, G. S. Mattioli, P. E. Jansma, and T. Dixon (2007), Kinematics of the Nicaraguan forearc from GPS geodesy, *Geophys. Res. Lett.*, *34*, L02302, doi:10.1029/2006GL027586.

van Wyk de Vries, B. (1993), Tectonics and magma evolution of Nicaraguan volcanic systems, Ph.D. thesis, pp. 1–328, Open Univ, Milton Keynes, U. K.

Walker, J. A., M. J. Carr, L. C. Patino, C. M. Johnson, M. D. Feigenson, and R. L. Ward (1995), Abrupt change in magma generation processes across the Central American arc in southeastern Guatemala: Flux-dominated melting near the base of the wedge to decompression melting near the top

of the wedge, *Contrib. Mineral. Petrol.*, *120*, 378–390, doi:10.1007/BF00306515.

Weinberg, R. F. (1992), Neotectonic development of western Nicaragua, *Tectonics*, *11*, 1010–1017, doi:10.1029/92TC00859.

Wiens, D. A., and G. P. Smith (2003), Seismological constraints on structure and flow patterns within the mantle wedge, in *Inside the Subduction Factory*, *Geophys. Monogr. Ser.*, vol. 138, edited by J. Eiler, pp. 59–82, AGU, Washington, D. C.

Yang, X., K. M. Fischer, and G. A. Abers (1995), Seismic anisotropy beneath the Shumagin Islands segment of the Aleutian-Alaska subduction zone, *J. Geophys. Res.*, *100*, 18165–18,177, doi:10.1029/95JB01425.

Zhang, S., and S. Karato (1995), Lattice preferred orientation of olivine aggregates deformed in simple shear, *Nature*, *375*, 774–777, doi:10.1038/375774a0.

Zimmerman, M. E., S. Q. Zhang, D. L. Kohlstedt, and S. Karato (1999), Melt distribution in mantle rocks deformed in shear, *Geophys. Res. Lett.*, *26*, 1505–1508, doi:10.1029/1999GL900259.